Available online at www.sciencedirect.com

ScienceDirect

Geochimica et Cosmochimica Acta 229 (2018) 1–19

Geochimica et Cosmochimica Acta

www.elsevier.com/locate/gca

Microstructural and paleomagnetic insight into the cooling history of the IAB parent body

Claire I.O. Nichols [a,*], Robert Krakow [b], Julia Herrero-Albillos [c,d], Florian Kronast [e], Geraint Northwood-Smith [a], Richard J. Harrison [a]

[a] Department of Earth Sciences, University of Cambridge, Downing Street, Cambridge CB2 3EQ, United Kingdom
[b] Department of Materials Science and Metallurgy, University of Cambridge, 27 Charles Babbage Road, Cambridge CB3 0FS, United Kingdom
[c] Centro Universitario de la Defensa, Zaragoza 50090, Spain
[d] Instituto de Ciencia de Materiales de Aragon, Departamento de Física de la Materia Condensada, Consejo Superior de Investigaciones Científicas, Universidad de Zaragoza, Zaragoza 50009, Spain
[e] Helmholtz Zentrum Berlin, Elektronenspeicherring BESSY II, Albert-Einstein-Strasse 15, Berlin 12489, Germany

Received 24 May 2017; accepted in revised form 7 March 2018; available online 15 March 2018

Abstract

The IABs represent one of only two groups of iron meteorites that did not form by fractional crystallization of liquid Fe-Ni in the core of a differentiated planetesimal. Instead, they are believed to originate from a partially differentiated body that was severely disrupted by one or more impacts during its early history. We present a detailed microstructural and paleomagnetic study of the Odessa and Toluca IAB meteorites, with a view to further constraining the complex history of the IAB parent body. X-ray photoemission electron microscopy and energy dispersive spectroscopy were used to generate high-resolution Ni/Fe maps. The crystallographic architecture of Odessa was analysed using electron backscatter diffraction. Paleomagnetic signals and the magnetic properties of several microstructures were also assessed using X-ray magnetic circular dichroism. Odessa exhibits a complex series of microstructures, requiring an unusual evolution during slow cooling. A conventional Widmanstätten microstructure, consisting of multiple generations of kamacite lamellae surrounded by M-shaped diffusion profiles, developed via continuous precipitation to temperatures below ~400 °C. Multiple generations of pearlitic plessite nucleated from kamacite/taenite ($T > 400$ °C) and tetrataenite rim/taenite interfaces ($T < 400$ °C), via a process of discontinuous precipitation. Rounded rafts of Ni-rich taenite, observed within some regions of pearlitic plessite, are shown to have the same crystallographic orientation as the parental taenite, and a non-standard orientation relationship with the enclosing kamacite. Contrary to current theories, these rafts cannot have formed by coarsening of pre-existing pearlitic plessite. A new bowing mechanism is proposed, whereby rafts of Ni-enriched taenite form between advancing lobes of an irregular reaction front during discontinuous precipitation. Subsequent coarsening leads to the growth of the taenite rafts, and the partial or complete removal of pearlite lamellae, resulting in spheroidised plessite with a crystallographic architecture matching the experimental observations. We find no evidence for a strong magnetic field on the IAB parent body, suggesting it did not have an active core dynamo at the time of cloudy zone formation. This supports the prediction that the IAB parent body was unable to form a significant core due to the redistribution of metal during an earlier impact event.

Keywords: IAB iron meteorites; Paleomagnetism; Cloudy zone; X-PEEM; EBSD; Microstructures; Pearlitic plessite; Spheroidised plessite; Thermal evolution

* Corresponding author.
E-mail address: cion2@cam.ac.uk (C.I.O. Nichols).

https://doi.org/10.1016/j.gca.2018.03.009
0016-7037/

1. INTRODUCTION

The parent bodies of meteorites are traditionally defined as either fully undifferentiated or fully differentiated (Weisberg et al., 2006). The IABs are an unusual group of iron meteorites that have been proposed to come from a partially differentiated body; they show contrasting chemical compositions to the other iron groups (except the IIEs) and do not appear to have formed by fractional crystallisation of a bulk source melt (Wasson and Kallemeyn, 2002; Goldstein et al., 2009; Benedix et al., 2014). They also contain silicate fragments of chondritic and primitive achondritic composition, including basaltic, troctolitic and peridotitic compositions, suggesting silicates within the parent body did not all experience the same degree of differentiation (Benedix et al., 2000). The IABs form several subgroups, which are both isotopically and chemically distinct. It is still a matter of debate whether these subgroups represent isolated pools of metal in one parent body, or represent several separate parent bodies (Worsham et al., 2016, 2017).

The IABs have a complex history, which is, in part, well constrained by isotopic dating and petrologic observations. Hf-W measurements suggest an accretion age ~2 Myr after calcium-aluminum-rich inclusions (CAIs) and metal-silicate segregation ~5 Myr after CAIs (Schulz et al., 2012). Ruzicka (2014) suggests segregation occurred during an initial impact event, which caused partial reheating of the asteroidal parent body, generating small amounts of silicate and metallic melt. An incipient core was then able to segregate, surrounded by a silicate mantle hypothesised to be the source of the Winonaites – a group of primitive achondritic meteorites (Greenwood et al., 2012). The body is assumed to be insulated by a thick chondritic layer from petrological and cooling rate observations (Rasmussen, 1989; Benedix et al., 2000; Takeda et al., 2000; Goldstein et al., 2014). Benedix et al. (2000) used two-pyroxene thermometry to argue that silicates reached a maximum temperature of ~1250 °C during accretion. This is supported by the lack of evidence for extensive melting or fractionation of the IAB silicates. This suggests that a sulphur-enriched core was formed by low degrees of partial melting (Benedix et al., 2014). The metal separates from the silicates when it reaches its eutectic (~85 wt% FeS) at 950 °C for the Fe-Ni-S system (Benedix et al., 2014) or 990 °C for the Fe-FeS system (Qin et al., 2008). Silicate metamorphism and resetting of low-temperature chronometers suggest a large impact event occurred ~8.5–17 Myr after CAIs (Schulz et al., 2012). This is also supported by the highly variable cooling rates and distinct chemical trends of IAB metal, suggesting formation in isolated metal pools throughout the parent body. This early 'scrambling' impact event occurred whilst the metal within the planetesimal was still molten; Re-Os isotope studies suggest metal solidification began 38 ± 21 Myr after CAIs (Horan et al., 1998). The scrambling impact redistributed silicate material, removing the outermost part of the body. The high metal content of the IABs suggests that an incipient metallic core remained, or ductile remobilization allowed the metal to form large pools (Ruzicka, 2014). Once scrambled, metal in the IAB parent body cooled and crystallized. At low temperatures ($\lesssim$780 °C) cooling rates were 63–650 °C Myr^{-1}, dropping to 1–20 °C Myr^{-1} at temperatures below 500–600 °C (Rasmussen, 1989). Cooling rates were determined using the central Ni concentration versus taenite width. This is consistent with estimates from Ni diffusion modelling, suggesting cooling on the order of ~10 °C Myr^{-1} (Yang et al., 2010). A recent Mo, Hf and Os isotope study of the IABs suggests an even more complex formation history, with subgroups forming on up to four parent bodies, each of which experiences a varying degree of internal heating and multiple impact events (Worsham et al., 2017).

There are still several open questions: Do the various IAB subgroups originate from a single parent body or from multiple parent bodies? Did the IAB parent body differentiate enough to form a significant metallic core? Did that core generate a dynamo? How many impact events influenced the evolution of the parent body, and is it possible to distinguish between them? IAB meteorites exhibit the Widmanstätten pattern, commonly observed in polished and etched sections of iron meteorites (Harrison et al., 2017). In addition, atypical microstructures such as spheroidised and pearlitic plessite are commonly observed in IAB meteorites (Buchwald, 1975).

We discuss three microstructures in detail in this paper: the cloudy zone, spheroidised plessite and pearlitic plessite. The cloudy zone (Fig. 1d) forms during slow cooling (<10,000 °C Myr^{-1}) (Yang et al., 2010) of taenite compositions between 25 and 47 Ni wt% (Yang et al., 1996). The taenite cools into a spinodal region below 450 °C at which point it decomposes into islands with composition $Fe_{0.5}Ni_{0.5}$ and a diameter of 10–500 nm, depending on cooling rate, surrounded by an Fe-rich matrix.

Spheroidised plessite consists of taenite spheroids and lamellae in a kamacite host (Fig. 1c). The spheroids are the most Ni-rich component, and are of order 5–10 μm in diameter. Narrow taenite lamellae with a slightly lower Ni content have one consistent orientation and are often interconnected to the spheroids.

Pearlitic plessite is a two-phase lamellar intergrowth of kamacite and taenite (Fig. 1a and b). Lamellae are of order of one micron in thickness and grow at a high angle from the tetrataenite rim. The taenite lamellae typically have a slightly higher Ni content than the surrounding taenite, and the kamacite a slightly lower Ni content.

The origin and significance of these atypical microstructures is poorly understood. We present a detailed high-resolution electron backscatter diffraction (EBSD) and X-ray photoemission electron microscopy (X-PEEM) study of the Odessa Main Group IAB iron, with particular focus on evaluating potential formation mechanisms for spheroidised and pearlitic plessite. EBSD is emerging as a powerful tool to study the formation and history of extraterrestrial materials (Forman et al., 2017). We discuss the composition, textures, crystallographic architecture and magnetic properties of the various Fe-Ni microstructures found, with the aim of further constraining the cooling and impact history of the IAB parent body/bodies during the time between metal solidification and its final breakup.

Paleomagnetic analysis of the cloudy zone was also carried out on both Odessa and Toluca. The cloudy zone has

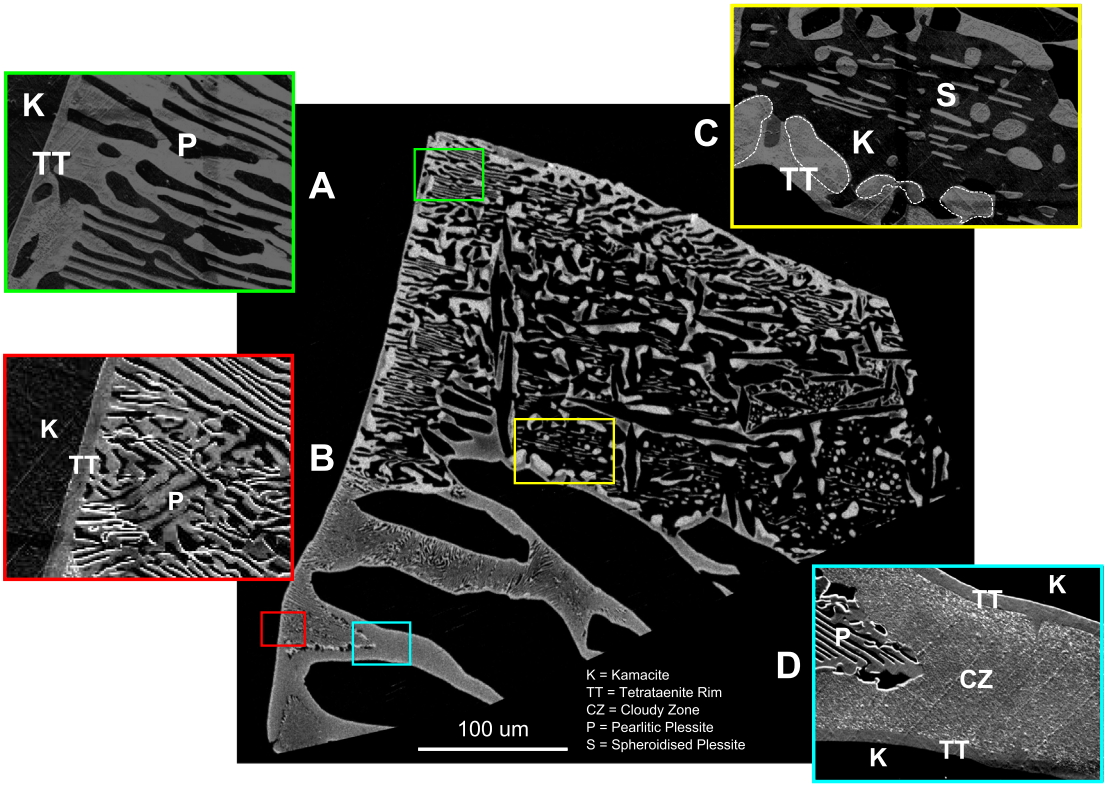

Fig. 1. Overview backscatter electron (BSE) Ni/Fe map of the microstructures in Region 2 of Odessa. Bright regions are Ni-rich and dark regions are Fe-rich. The microstructures which will be discussed in this paper have all been highlighted and are as follows: kamacite (K), tetrataenite rim (TT), cloudy zone (CZ), pearlitic plessite (P) and spheroidised plessite (S). (a) A region of coarse pearlitic plessite. (b) A region of fine pearlitic plessite. (c) A region of spheroidised plessite and irregular taenite rafts highlighted by white dashed lines. (d) A region of cloudy zone and its interface with fine pearlitic plessite.

been shown to have unique capabilities as a paleomagnetic recorder (Bryson et al., 2014a, 2015; Nichols et al., 2016). Isolated islands of tetrataenite within the cloudy zone become magnetised as they grow, acquiring a chemical transformation remanent magnetisation (CTRM). Their extremely high coercivity >2 T (Uehara et al., 2011) suggests that, once magnetised, these islands provide a robust magnetic history, immune to alteration or magnetic overprints. We image the magnetisation direction of tetrataenite islands in the cloudy zone of both Odessa and Toluca using X-PEEM combined with X-ray Magnetic Circular Dichroism (XMCD). Our results suggest that the IAB parent body did not have an active core dynamo at the time of cloudy zone formation.

2. METHODS

2.1. Sample preparation

Two samples of IAB iron meteorites, Odessa (11538) and Toluca (TN 4389) were obtained from the Sedgwick Museum, University of Cambridge. Samples were cut to 5×5 mm sections using a tile cutting saw and ground down using a lapping wheel, in the presence of flowing cold water to prevent heating. Samples were polished using progressively finer grade diamond pastes from 9 μm to 0.25 μm and etched using nital. Etched surfaces were inspected using a reflected light microscope to look for signs of alteration or shock. Samples were then thinned to 1 mm thickness using coarse polishing paper, and the top surface was repolished down to 0.25 μm diamond paste.

2.2. Microstructural analysis

Scanning electron microscopy (SEM) was carried out using an FEI Quanta 650 field-emission SEM in the Department of Earth Sciences, University of Cambridge. Large areas of Odessa were imaged at high spatial resolution using the stage mapping software MAPS (FEI Software). Secondary electron (SE) and backscattered electron (BSE) images were acquired with a dwell time of 5 μs in high-vacuum mode with an accelerating voltage of 2 kV and a working distance of 8 mm.

EBSD imaging of the BSE mapped regions utilised an acceleration voltage of 20 kV, working distance of 24.4 mm and a sample tilt of 70°. Results were indexed and plotted using Bruker software (ESPRIT 2) for body-centred cubic (bcc) iron (phase group $Im\bar{3}m$, a = 2.866 Å), and face-centred cubic (fcc) iron ($Fm\bar{3}m$, a = 3.639 Å). Detailed analysis of the indexed dataset was done offline with the Matlab toolbox *MTEX* (Bachmann et al., 2010). Crystallo-

graphic orientations of selected kamacite grains were plotted in (1 0 0) and (1 1 0) pole figures to check for common poles. *MTEX* was used to plot kamacite and taenite orientations in the respective 3D fundamental zone (axis-angle representation) to inspect the raw EBSD data (Frank, 1988; Morawiec, 1997; Krakow et al., 2017). A fundamental zone is the domain where each symmetry-equivalent orientation or misorientation occurs only once. The domain geometry is characteristic for the symmetry operators of the combined crystal symmetries. Here the following two fundamental zones are used: a truncated cube for cubic orientations (applying cubic symmetry operators once) and 1/24 of the truncated cube (applying cubic symmetry twice).

Grain and phase boundary misorientations were computed using *MTEX* by first identifying grains (threshold: 5°) and second by calculating the misorientation at each grain boundary segment using kamacite as the reference frame. A boundary misorientation is the rotation needed to bring the reference frames of the two orientations at either side of the boundary into coincidence. In other words, a misorientation is the rotation between two orientations. This rotation can be expressed in several ways (Bunge, 1982). Here the axis-angle representation is chosen since it is easy to recognise the vectors corresponding to an axis-angle pair (Frank, 1988; Morawiec, 1997). Grain and phase boundary misorientations were subsequently plotted in the appropriate fundamental zone to highlight phase relationships (orientation relationships). By following this workflow we are able to utilise the entire EBSD dataset, correlating spatial, orientation and misorientation information.

Energy-dispersive spectroscopy (EDS) was used to acquire elemental maps for Fe, Ni, C and P in high-vacuum mode at an accelerating voltage of 20 kV and working distance of 24.4 mm (Figs. S1–S4). EDS data were combined with EBSD results to map the crystallographic orientations directly onto the phase map. EDS data were analysed with ESPRIT 2. Features of interest were manually selected on the BSE image as polygons, lines or points (Fig. S5). The composition of the regions of interest were quantified using Bruker ESPRIT software. We use standardless P/B-ZAF quantitative analysis to assess both X-ray peaks and bremsstrahlung background (Pouchou and Pichoir, 1991; Labar and Torok, 1992). X-ray peaks are automatically identified by manually selecting the elements of interest, in this case Fe and Ni (Fig. S6). The background is manually selected by identifying regions of noise between distinct peaks. A quantification estimate is then calculated by the ESPRIT software. Only features larger than ~10 μm can be quantified, therefore this method is better for analysing the average composition of microstructures, rather than the phases they consist of.

2.3. X-ray photoemission electron microscopy and X-ray magnetic circular dichroism

Samples of both Toluca and Odessa were measured at the SPEEM UE49 beamlime, BESSY II, Berlin (Kronast et al., 2010). We follow the same methodology as described by Bryson et al. (2015) and Nichols et al. (2016). Two samples of Odessa and one of Toluca were measured. Samples were initially sputtered using Ar ions under vacuum ($P < 1.5 \times 10^{-5}$ mbar) to remove oxidation and magnetisation effects due to surface polishing. Toluca and the two samples of Odessa were sputtered for 23 h, 20.5 h and 18.5 h, respectively, whilst reducing the voltage in discrete steps from 1.2 keV to 0.4 keV in order to minimise surface topography. Samples were held in vacuum between sputtering and measuring. Measurements were performed under a vacuum of $P < 1 \times 10^{-8}$ mbar.

Compositional images were acquired using X-PEEM. Horizontally polarised X-rays were tuned to the Fe-L_3 and Ni-L_3 edges (707 eV and 852 eV, respectively), preferentially exciting secondary photoelectrons from the top ~ 5 nm of the sample surface (Nolting et al., 2000; Ohldag et al., 2001). Pre-edge images were also acquired (700 eV and 845 eV for Fe and Ni, respectively) and these were used to normalise the L_3-edge images. The image acquired at the Ni-L_3 edge was then divided by the image acquired at the Fe-L_3 edge in order to maximise contrast. The resulting images represent semi-quantitative maps of relative Ni/Fe ratio. A 10 μm field of view was used in all cases, with a maximum achievable resolution of 30 nm (Locatelli and Bauer, 2008).

Both horizontally- and circularly-polarised X-rays are used to image the composition and magnetisation in the same region, providing a directly comparable field of view. Magnetisation is imaged using XMCD at the Fe-L_3 edge, for both left- and right- circularly polarised X-rays. Nine, six and fifteen regions were imaged for Toluca and the two Odessa samples, respectively.

2.4. Paleomagnetic analysis

For analysis of XMCD images, we split the cloudy zone into discrete regions parallel to the tetrataenite rim – cloudy zone interface. A histogram of XMCD pixel intensity was generated for each region. Tetrataenite islands in the cloudy zone can be magnetised along one of three orthogonal easy axes (the crystallographic axis along which magnetisation is ideally aligned), resulting in six distinct XMCD intensities corresponding to positive (blue) and negative (red) signals along each of these easy axis directions. The XMCD intensity is directly proportional to the projection of magnetisation along the X-ray beam (Bryson et al., 2014b). If no magnetic field was present when the cloudy zone acquired its CTRM, the distribution of magnetisation directions during the formation of the cloudy zone should be entirely random, corresponding to a normally-distributed histogram of pixel intensity centred at zero.

Since we are considering relatively small populations of just hundreds of islands within the cloudy zone, the variability within a random distribution is significant. We account for this variability by generating random distributions for analogous synthetic data sets. The six XMCD intensities corresponding to the three easy axis orientations (for both positive and negative magnetisation directions) are quantified in the tetrataenite rim for each image, by manually selecting distinct magnetic domains and fitting a Gaussian curve to their pixel intensity distribution. These six intensities are then randomly assigned to an array with

the same number of points as the number of islands within a region of interest in the cloudy zone. The number of points is calculated by dividing the area of the region of interest by the size of the islands. The process is repeated to reflect the number of images collected in the experimental data; for example, there are nine repeats for Toluca. The average of the set of random distributions is then calculated, and the process repeated ten thousand times. The resulting distribution represents the variability in a random distribution for the specific conditions analogous to the experimental data set. If the average of the histogram of XMCD intensity lies within two standard deviations of the random distribution then the histogram cannot be distinguished from a random distribution, implying zero magnetic field to 95% confidence.

3. RESULTS

3.1. Microstructural analysis

A BSE overview of the microstructures present in Odessa is shown in Fig. 1. The darkest signals are from bcc kamacite, the most Fe-rich phase, containing ~5–7 wt % Ni (see Table 1). Brighter signals are from fcc taenite, containing ~14–48 wt% Ni. We note abundant rhabdite ($(Fe, Ni)_3P$) crystals visible in Fig. S8 and larger schreibersite crystals observed in Fig. S10. The overview image focusses on a patch of retained taenite, surrounded on all sides by first-generation kamacite. As kamacite grew, Ni was increasingly partitioned into the retained taenite, causing a build-up of Ni in this region. As cooling continues, smaller second- and third-generation kamacite lamellae nucleated inside the retained taenite, creating further redistribution of Ni on ever decreasing length scales.

Immediately adjacent to each kamacite lamella we observe a clear tetrataenite rim. In some regions, the tetrataenite rim is immediately followed by cloudy zone (Fig. 1d). In other regions, however, the tetrataenite rim is followed by pearlitic plessite (Fig. 1a and b). Pearlitic plessite forms predominantly around the edges of the retained taenite, and sometimes nucleates directly off the surrounding kamacite. The spacing of the lamellae within pearlitic plessite is highly variable, but can be broadly subdivided into coarse (Fig. 1a) and fine (Fig. 1b) regions, with lamellar spacing ~1–1.5 μm and <0.5 μm, respectively. It is noteworthy that the coarsest lamellae are observed to be those nucleating directly off the kamacite/taenite boundary. Irregular patches of Ni-rich taenite are commonly observed along the edges of the retained taenite, sandwiched between the cloudy zone and the coarse pearlite, with some appearing as islolated rafts embedded within the coarse pearlite. These rafts become smaller and more rounded towards the centre of the retained taenite, where spheroidised plessite (Fig. 1c), rather than pearlitic plessite, is more commonly observed.

The Fe-Ni microstructures observed in the Odessa and Toluca IAB meteorites vary significantly on a μm scale. Selected examples of the observed microstructural variability are illustrated in the X-PEEM Ni/Fe maps (Fig. 2). The morphology of pearlitic plessite varies from coarse, graphic-like features (such as those observed in granites)

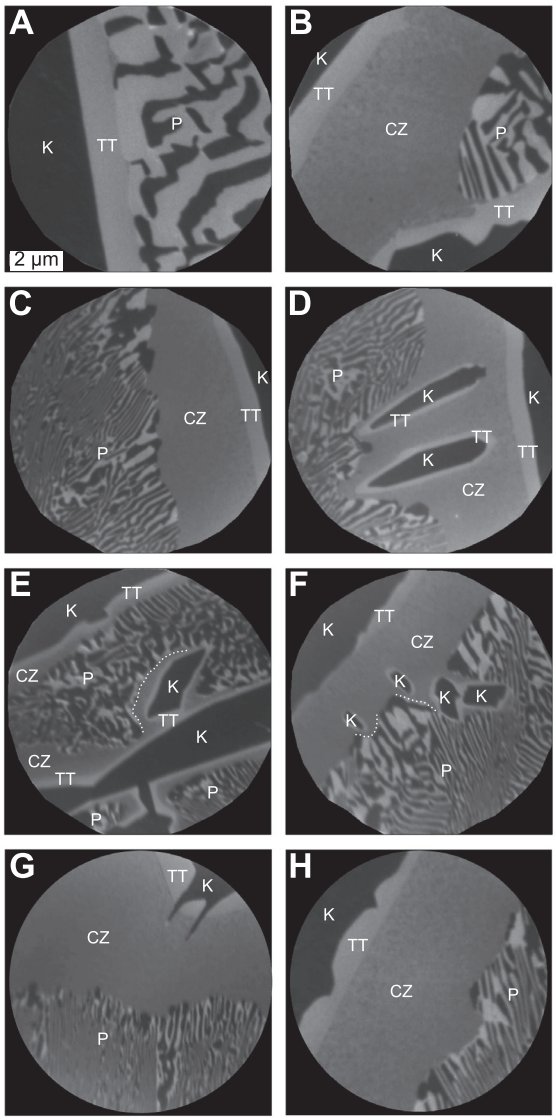

Fig. 2. X-PEEM images to show the full range of microstructural heterogeneity observed in the Toluca and Odessa meteorites. Images were taken a few μm apart. Dark regions are Fe-rich whilst bright regions are Ni-rich. K = kamacite, TT = tetrataenite rim, CZ = cloudy zone and P = pearlitic plessite. (a) Microstructures in Toluca. (b)–(h) Microstructures in Odessa. Deflection of pearlitic plessite by kamacite rhombs is highlighted by white dotted lines.

(Fig. 2a) to coarse and fine lamellae (Fig. 2b, c, d, and f) and a more irregular structure (Fig. 2e). It is unclear what controls the morphology in each case, however the angle of the intergrowth to the surrounding interface is useful for identifying the nucleation surface. In the cases where pearlitic plessite has a boundary with the tetrataenite rim, the lamellae are often oriented close to perpendicular to the rim, suggesting the rim acted as the nucleation surface from which the kamacite/taenite reaction-front advanced (e.g. Fig. 1a). The interfaces between the pearlitic plessite and the cloudy zone tend to be far more irregular, and the orientation of the pearlitic plessite is not controlled by

the interface. Compositional profiles were taken across regions of pearlitic plessite. The kamacite and taenite lamellae in pearlite are more Ni-rich than the bulk kamacite and tetrataenite rim, respectively (Fig. S7).

Small μm-scale kamacite rhombs are found within regions of cloudy zone and plessite (Fig. 2d–f). Each kamacite rhomb is associated with an M-shaped diffusion profile, and is rimmed by tetrataenite (Fig. S9). A common feature is the apparent deflection of the advancing pearlitic plessite around the kamacite rhombs (Fig. 2d–f). This deflection often occurs at a considerable distance, suggesting the kamacite rhomb influences the Ni diffusion profile in the surrounding region.

The interfaces between kamacite and the tetrataenite rim, the tetrataenite rim and the cloudy zone and the tetrataenite rim and pearlitic plessite show a high degree of variability. In some cases they are straight and parallel, whereas in other cases they are highly irregular (Fig. 2). There are several examples of one phase entirely cross cutting another, particularly evident in cases where kamacite entirely cross cuts the tetrataenite rim, puncturing the cloudy zone (Fig. 2d, f, and g).

3.2. EBSD analysis

EBSD results for Region 2 of Odessa are summarised in Fig. 3, which shows the orientation of both kamacite and taenite phases. A second region was also analysed yielding similar results (Odessa Region 1, Fig. S11). The locations and relationship between Region 1 and Region 2 are shown in Fig. S10. Retained taenite (yellow, labelled γ) is surrounded by first-generation kamacite (red, labelled α), containing occasional Neumann bands (light blue, labelled NB). The orientation of the tetrataenite rim is identical to the orientation of the retained taenite, consistent with findings from a detailed EBSD study by Goldstein and Michael (2006). The two different phases are indistinguishable in an EBSD map due to the similarity of their crystal structure and their EBSD patterns. The retained taenite is subdivided by a finer-scale Widmanstätten pattern of differently orientated kamacite lamellae (labelled α_{W1} and α_{W2}), patches of coarse and fine pearlitic plessite, irregular patches and rafts of Ni-rich taenite, and spheroidised plessite. Spheroidised plessite contains both taenite spheroids (yellow), with identical crystallographic orientation to the retained taenite, and thin taenite lamellae (green and orange), with a different orientation to the retained taenite. Both the taenite spheroids and thin taenite lamellae are embedded in a kamacite host which displays remarkably uniform crystallographic orientation across the central region (light blue/grey). Like the taenite spheroids, the irregular rafts of Ni-rich taenite observed around the edges of, and embedded within, the coarse pearlite, also have identical crystallographic orientation to the retained taenite).

The phase boundary between first/s/third-generation kamacite laths and the surrounding taenite/tetrataenite obeys the Kurdjumov-Sachs (KS) relationship (Kowalik et al., 1988), with the closest-packed plane of the kamacite

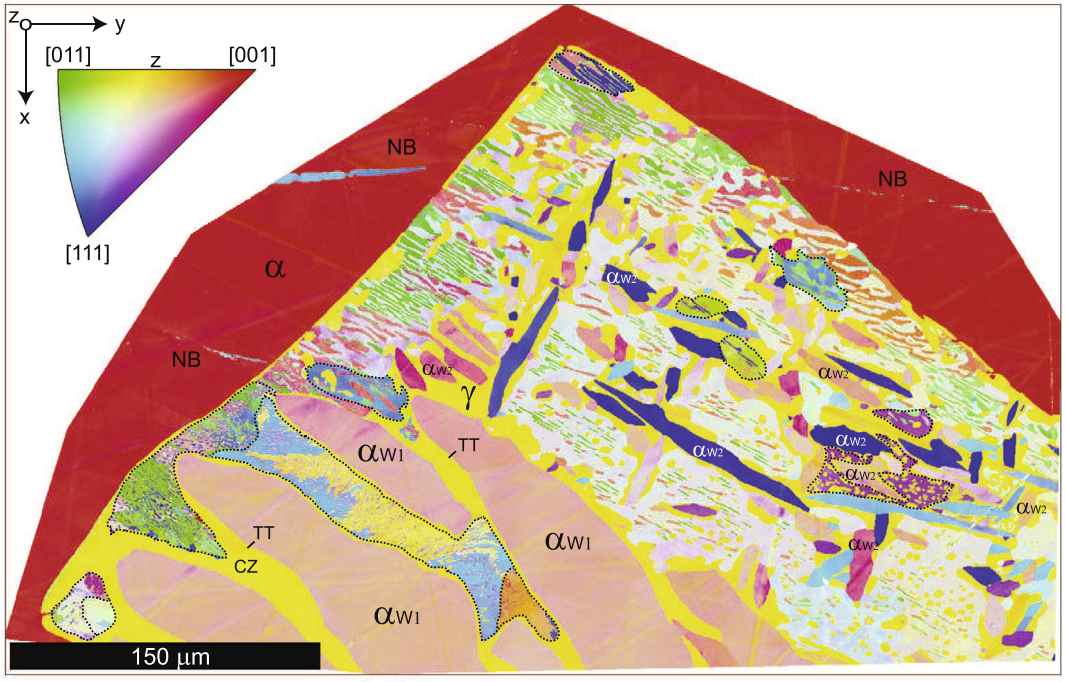

Fig. 3. EBSD inverse pole figure for Region 2 of the Odessa meteorite, showing the crystallographic orientation of both kamacite and taenite. Colours correspond to inverse pole figure directions with respect to the z-axis (normal to the image plane). The orientation map shows the first-generation kamacite (α) and retained taenite (γ) in red and yellow, respectively, which are both homogeneous in orientation. Selected second- and third-generation kamacite laths are labelled α_{W1} and α_{W2} (Table 2). Neumann bands (NB), tetrataenite rim (TT) and cloudy zone (CZ) are also indicated. Kamacite subgrains with different crystallographic orientations are highlighted by dotted lines. (For interpretation of the references to colour in this figure legend, the reader is referred to the web version of this article.)

Table 1
Compositions of the cloudy zone and pearlitic plessite estimated from average X-PEEM intensities. X-PEEM intensities are calibrated by fixing the composition of kamacite and the tetrataenite rim to EDS data. For regions where no cloudy zone composition is given the pearlitic plessite extends all the way to the tetrataenite rim. In these cases the Ni content of the pearlitic plessite is higher than when it occurs adjacent to the cloudy zone, consistent with an M-shaped Ni diffusion profile.

Meteorite	Kamacite (Ni wt% $\pm 1\sigma$)	Tetrataenite Rim (Ni wt% $\pm 1\sigma$)	Cloudy Zone (Ni wt% $\pm 1\sigma$)	Pearlitic Plessite (Ni wt% $\pm 1\sigma$)
Toluca	7.0 ± 0.2	48.6 ± 1.0	–	36.6 ± 0.4
	7.0 ± 0.2	48.6 ± 1.0	–	35.6 ± 0.1
	7.0 ± 0.2	48.6 ± 1.0	–	32.8 ± 1.0
	7.0 ± 0.2	48.6 ± 1.0	33.3 ± 0.1	28.2 ± 0.5
	7.0 ± 0.2	48.6 ± 1.0	30.4 ± 0.7	22.2 ± 0.8
	7.0 ± 0.2	48.6 ± 1.0	31.9 ± 0.9	26.9 ± 0.3
Odessa	7.0 ± 0.2	48.6 ± 1.0	29.7 ± 0.6	20.6 ± 0.5
	7.0 ± 0.2	48.6 ± 1.0	33.0 ± 0.3	29.1 ± 0.3
	7.0 ± 0.2	48.6 ± 1.0	30.2 ± 0.7	27.8 ± 0.7
	7.0 ± 0.2	48.6 ± 1.0	31.1 ± 0.7	19.7 ± 0.3
	7.0 ± 0.2	48.6 ± 1.0	35.7 ± 0.0	27.7 ± 0.1
	7.0 ± 0.2	48.6 ± 1.0	38.0 ± 0.1	31.5 ± 0.1

$\{0\ 1\ 1\}_{bcc}$ running almost parallel to the close-packed plane $\{1\ 1\ 1\}_{fcc}$ of taenite (Table 3). This was deduced by plotting the boundary misorientations across the kamacite-taenite boundary in the appropriate fundamental zone (axis-angle representation) and comparing their position with known relationships (Fig. 4a). This approach is quicker and more accurate than the use of several simultaneous pole figures. The KS orientation relationship was identified by a strong clustering of misorientation data around the KS point (red dot, Fig. 4b), which includes 77% of the data within a radius of 5°. For comparison, the position of the Bain (yellow), Nishiyama-Wassermann (blue) and Pitsch (green) orientation relationships are also shown in Fig. 4b (Table 3).

Fine pearlitic plessite forms a patchwork of domains with random orientations (e.g. P1-4 in Fig. 5), suggesting nucleation occurred independently at varying points along the tetrataenite rim. For a given domain of pearlitic plessite, kamacite adopts a more uniform crystallographic orientation (Fig. 5a) in comparison to the interleaving taenite

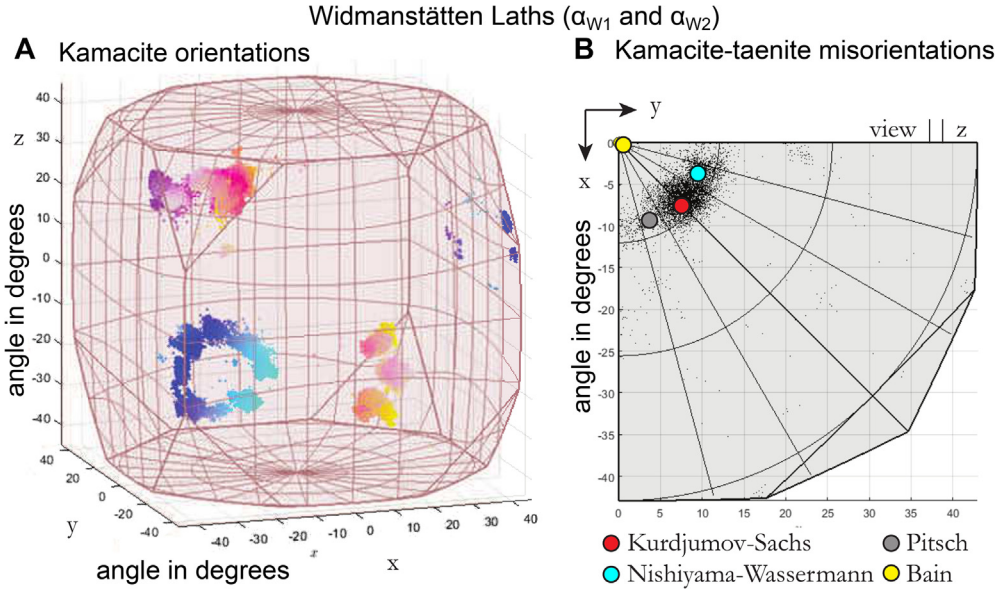

Fig. 4. Crystallographic relationship between the Widmannstätten bcc kamacite and its surrounding fcc taenite in Odessa. (a) Three ring-shaped clusters in the kamacite orientation space hint towards the Kurdjumov-Sachs orientation relationship with the taenite parent grain. The colours of the three sets of kamacite laths in the orientation map (Fig. 3) correspond with the colours of the three distinct ring-shaped clusters. (b) A convenient way to identify the kamacite-taenite phase relationship is to plot the boundary misorientations in misorientation space (axis-angle representation). The consistent strong relationship is evidenced by the cluster around the Kurdjumov-Sachs orientation relationship (red dot) which includes 77% of the data within a 5° radius. The position of the Bain (yellow), Nishiyama-Wassermann (black) and Pitsch (grey) orientation relationships are shown for comparison. (For interpretation of the references to colour in this figure legend, the reader is referred to the web version of this article.)

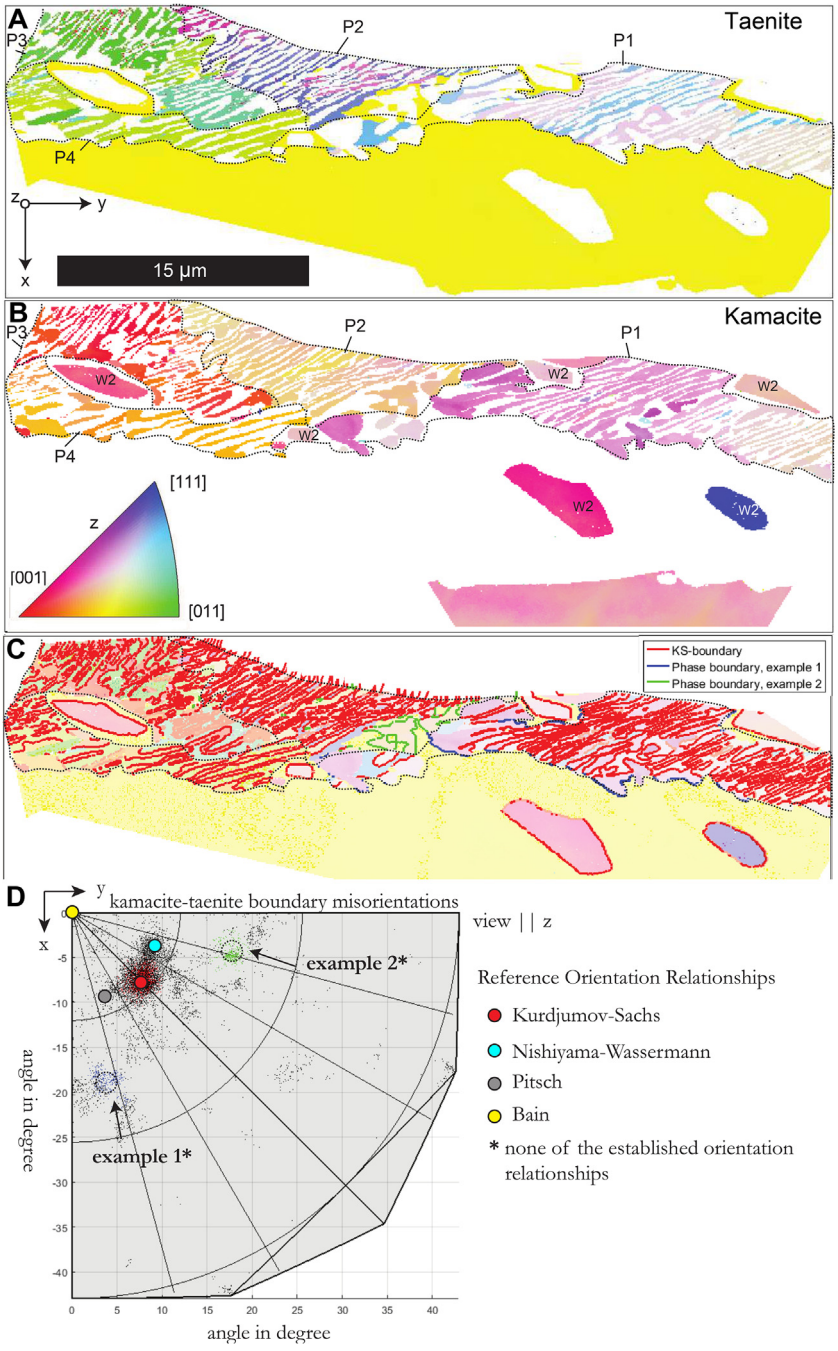

Fig. 5. Orientation map of pearlitic plessite region in Odessa. (a) Taenite phase (γ, fcc); the yellow regions are the tetrataenite rims. The stripes are the Ni-rich part of the pearlitic plessite. Crystallographic orientations of taenite in the pearlitic plessite are more heterogeneous than that of the kamacite phase. (b) Kamacite (α, bcc), colours indicate orientations as defined by the inverse pole figure. Larger blocky regions are kamacite rhombs (α_{W2}). The red/yellow/pink stripes are Fe-rich kamacite phase in pearlitic plessite and have fairly similar orientations for each grain (P1-P4). (c and d) Kamacite-taenite boundary misorientations in pearlitic plessite have a strong crystallographic relationship consistent with the KS relationship for the meandering boundary between the stripes (red line) but no special misorientation between pearlitic kamacite stripes and external taenite as shown for two examples (blue and green lines). As mentioned above the α_{W2} rhombs have the known KS relationship with the large taenite grain and the tetrataenite rim. (For interpretation of the references to colour in this figure legend, the reader is referred to the web version of this article.)

(Fig. 5b). The same observation can be made in several domains of pearlitic plessite highlighted with black dotted lines in the lower left hand part of Fig. 3. The KS orientation relationship was found between the meandering taenite and kamacite lamellae in pearlitic plessite for all domains, as indicated in red in Fig. 5c and d.

Misorientation analysis of the boundary between pearlitic kamacite and the tetrataenite rim suggests that there is no known orientation relationship between the two (Fig. 5c and d). This is shown for two boundaries called 'example1' and 'example2', highlighted in blue and green, respectively. This point is consistent with the fact that each kamacite domain in the plessite region (P1-P4) has a different orientation, which appears to have formed at random.

Spheroidised regions contain both taenite spheroids and thin taenite lamellae embedded in a kamacite host. The taenite spheroids have, without exception, the same crystallographic orientation as the retained taenite (yellow in Figs. 4 and 6). However, unlike other regions of retained taenite, they do not display a KS relationship with the surrounding kamacite. Misorientation analysis identifies two special spheroid-kamacite boundary relationships. The first boundary misorientation is prevalent in the majority of spheroids (green lines in Fig. 6) within the large white kamacite grain. The second (blue lines in Fig. 6) is observed only in an isolated patch of plessite (separate grain) that is entirely enclosed by second-generation kamacite lamellae.

Five observations are particularly relevant to determining the potential formation mechanism for kamacite in the spheroidised regions: (i) kamacite has no KS relationship with its surrounding retained taenite; (ii) kamacite has no KS relationship with the (embedded) taenite spheroids; (iii) the kamacite has a uniform morphology (no laths) and adopts a roughly uniform crystallographic orientation (light blue/grey colour in Fig. 3); (iv) closer examination using a restricted inverse pole figure (IPF) colour code reveals the presence of several interdependent subgrains with slightly different orientations (Fig. 7); (v) the kamacite orientation in spheroidised plessite is similar to that observed in neighbouring coarse regions of pearlitic plessite.

In close proximity to the taenite spheroids, thin taenite lamellae occur and adopt two distinct crystallographic

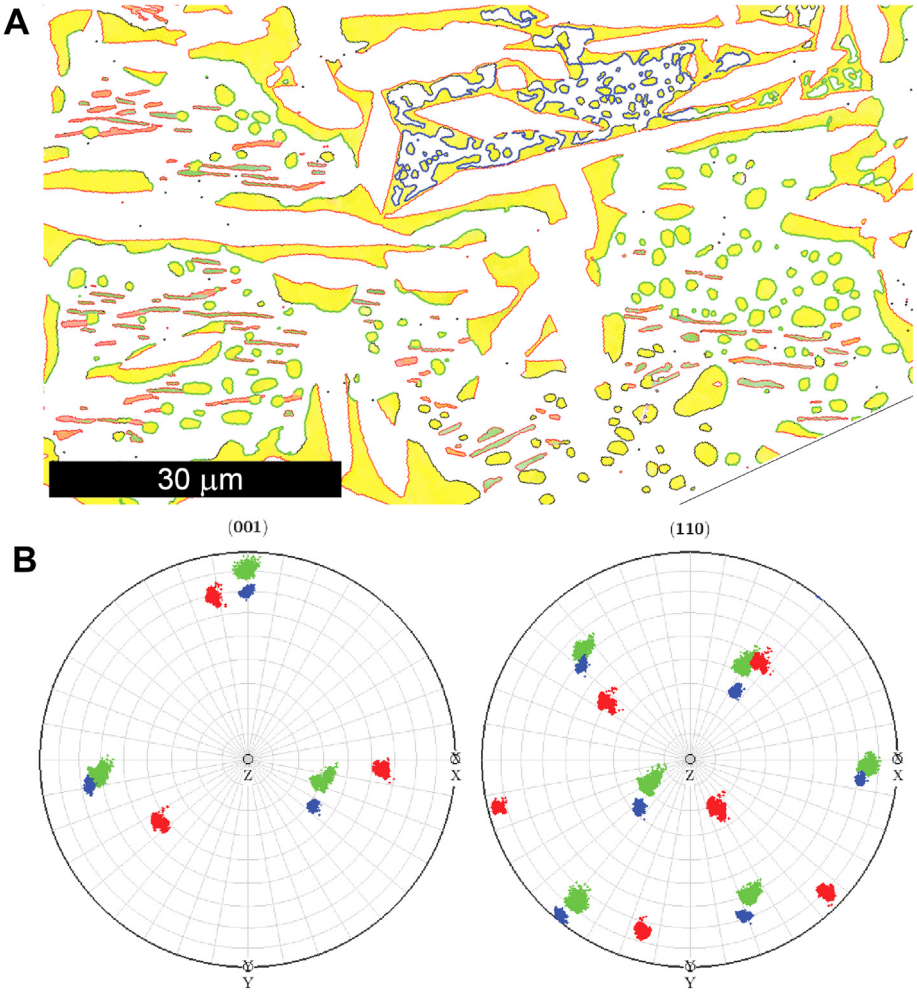

Fig. 6. Orientation map of a spheroidised plessite region. (a) Taenite phase (γ, fcc); the spheroids show two distinct, but similar types of misorientations with the respective surrounding kamacite. These two relationships are highlighted by the blue and green boundaries. The lamellae in the same region have a KS-type orientation relationship with the surrounding kamacite, represented by the red boundaries. (b) Pole figures projected along (0 0 1) and (1 1 0). The blue and green clusters show the distinct, but similar misorientations between the spheroids and the surrounding kamacite. The red clusters show the KS relationship the taenite lamellae have with the surrounding kamacite; this is clearly different to the blue and green misorientation clusters. (For interpretation of the references to colour in this figure legend, the reader is referred to the web version of this article.)

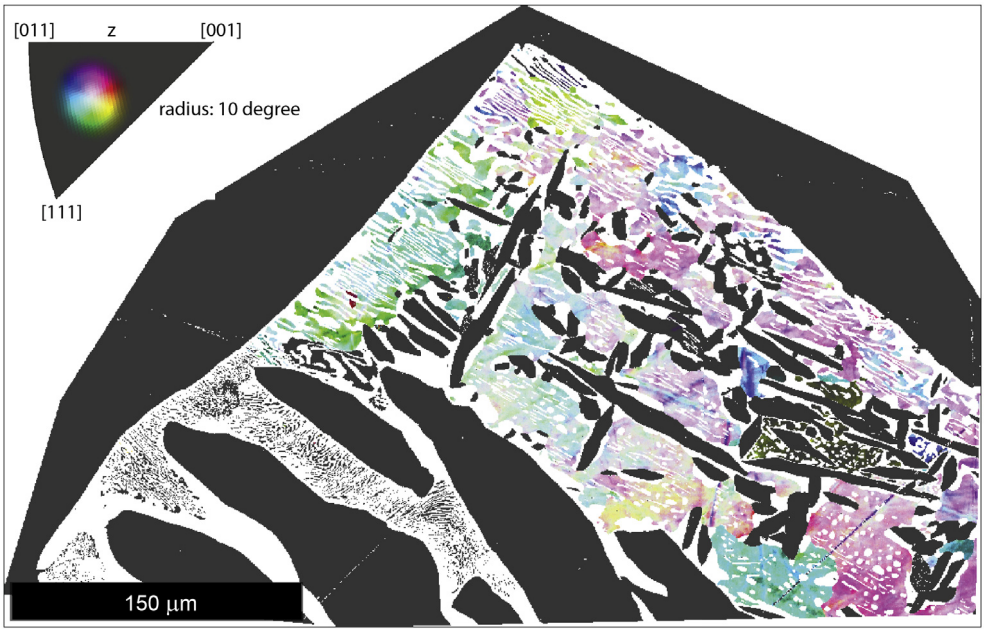

Fig. 7. Orientation map highlighting the subtle changes in crystallographic orientation of kamacite subgrains using a narrow colour code (cf. inlay, 10° radius). The presence of many interdependent subgrains may represent heterogeneity caused by interaction of a uniform external stress with the pre-existing kamacite exsolution lamellae.

orientations (green and orange) shown in Fig. 4, both of which have a KS orientation relationship with the surrounding kamacite host (red lines in Fig. 6). The same two orientations of taenite are observed in the coarse regions of pearlitic plessite.

3.3. Magnetic microstructure analysis

The XMCD intensities within each region of the cloudy zone for both Odessa and Toluca are normally distributed around zero (Fig. 8). In order to convert these XMCD intensities to paleointensities, the size of the islands in the cloudy zone must be known. Island size can be established from either direct measurement, or from cooling rate estimates, based on the empirically derived relationship between tetrataenite island diameter and cooling rate $d_{CZ} = \left(\frac{7.62\times10^6}{CR}\right)^{\frac{1}{2.9}}$, where d_{CZ} is the diameter of tetrataenite islands in the cloudy zone in nm, and CR is cooling rate in °C Myr^{-1} (Yang et al., 2010). Odessa has been reported to have a cooling rate of 0.5 °C Myr^{-1}, corresponding to a cloudy zone island diameter of ~300 nm (Rasmussen, 1989). Toluca has had the size of its islands directly measured, with a diameter of 120 nm, however more recent cooling estimates suggest its islands are slightly smaller, closer to 100 nm across (Winfield et al., 2012; Goldstein et al., 2014). We also note that the islands in the cloudy zone in Odessa do not look notably larger than those in Toluca in the X-PEEM images. We therefore use upper and lower bounds for each sample, 100–120 nm and 120–300 nm for Toluca and Odessa, respectively. We show that for both samples of Odessa and Toluca, even for the smallest island sizes, all XMCD histogram averages are well within the 95% confidence limit for zero magnetic field based on the statistical treatment outlined in Section 2.4. Since the error on zero magnetic field is so large, it is not possible to distinguish between zero magnetic field or a weak magnetic field; nor can we quantify a reliable paleointensity estimate. Therefore Toluca and Odessa are presented with relative paleointensities in Fig. 8d–f, by dividing the average XMCD intensity for each region of the cloudy zone by the volume of the tetrataenite islands. The same normalisation is applied to Toluca and Odessa so that a direct comparison can be made between samples.

X-PEEM and XMCD were used to image the composition and corresponding magnetisation of pearlitic plessite in both Toluca and Odessa. Pearlitic plessite exhibits strong XMCD intensities, suggesting the magnetisation is predominantly in-plane, consistent with soft multidomain behaviour (Fig. 9). The magnetic domains appear to be preferentially pinned to lamellar interfaces, however some magnetic domains crosscut the interfaces. The magnetisation of the tetrataenite rim shows a much closer correlation to the magnetisation of pearlitic plessite (Fig. 9b) than to the magnetisation of the cloudy zone (Fig. 9e). Multidomain magnetic behaviour is consistent with that observed in pearlite in steel (Hetherington et al., 1987; Van Wilderen et al., 2002).

XMCD imaging of kamacite reveals the presence of fine-scale magnetic domains, in addition to the more usual large-scale lamellar domains (Fig. S12). Such fine-scale domains are reminiscent of magnetic structures observed in materials with significant out-of-plane anisotropy, and have not been reported in any of the previous XMCD imaging studies of Fe-Ni meteorites (Bryson et al., 2014b,a, 2015; Nichols et al., 2016).

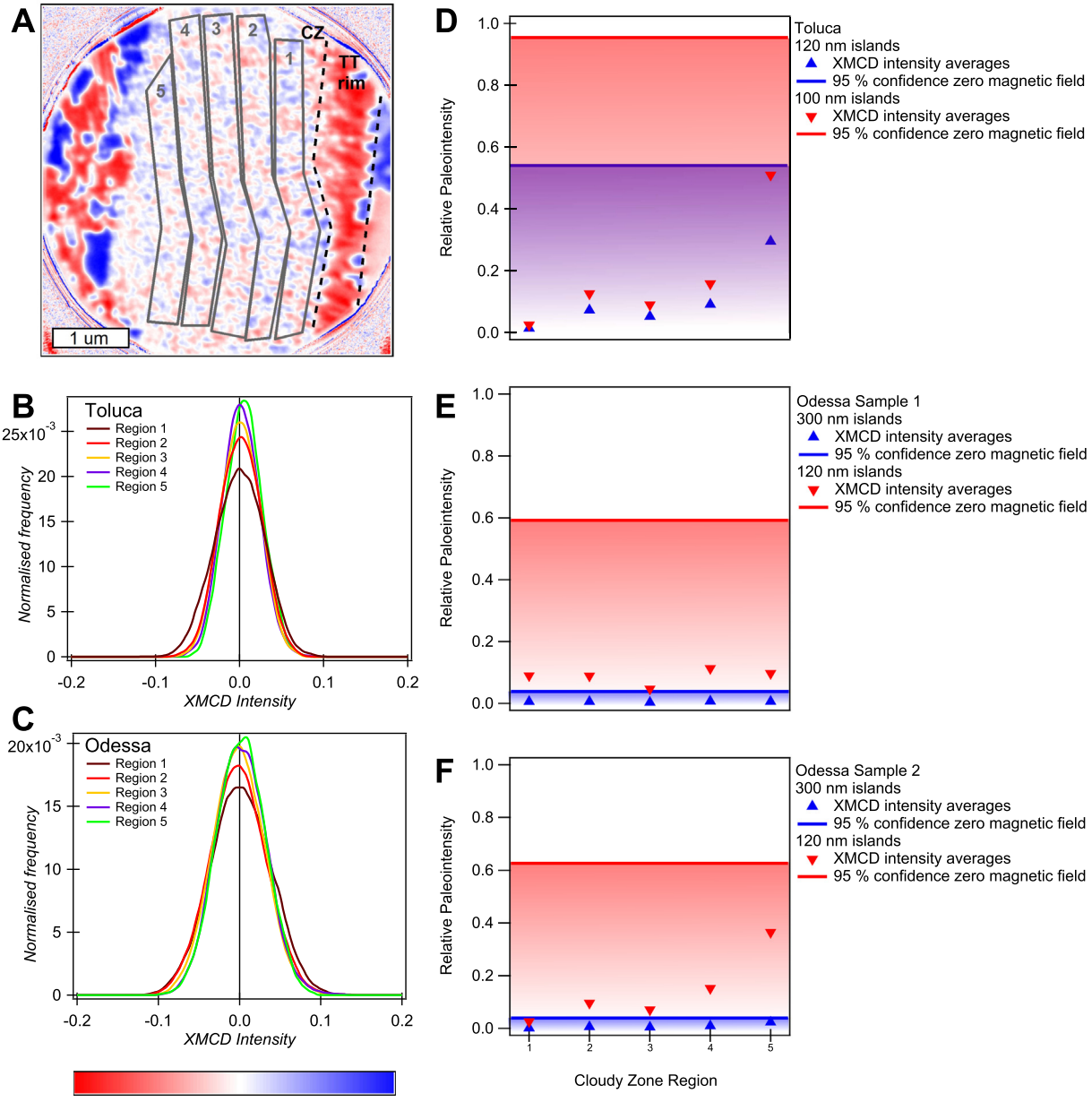

Fig. 8. (a) An example of an XMCD image from Toluca with each of the analysed regions of cloudy zone shown. Red represents magnetisation towards the direction of the X-ray beam, blue away from the X-ray beam and white perpendicular to the X-ray beam. For each region, a histogram of pixel intensity is generated, for Toluca (b) and Odessa (c). The five histograms represent the five regions of interest moving progressively further from the tetrataenite rim. All histograms show a normal distribution centred at zero. The average pixel intensity for each histogram is divided by the size of the islands in the cloudy zone to give a relative paleointensity. Red triangles represent the lower estimate on the paleointensity, for the largest size of cloudy zone islands whilst blue triangles represent the higher estimate on paleointensity for the smallest size of cloudy zone islands. The red and blue lines represent the upper bound on zero magnetic field to 95% confidence for 100 nm and 120 nm islands respectively for Toluca and 120 nm to 300 nm for Odessa. We show that for both Toluca (d) and Odessa (e & f), the relative paleointensity estimates lie within error of zero magnetic field. (For interpretation of the references to colour in this figure legend, the reader is referred to the web version of this article.)

4. DISCUSSION

4.1. Current theories on the formation of pearlitic and spheroidised plessite

Pearlitic plessite has been observed in several groups of meteorites including the IAB and IIICD irons and the L-group ordinary chondrites (Scott and Bild, 1974; Bennett and McSween, 1996), but its origin is poorly understood. Kowalik et al. (1987) studied the Dayton IAB iron and noted that the lamellar regions are depleted in phosphorous. They suggest this causes supersaturation of taenite, which precipitates to form the observed lamellae when entering the kamacite-taenite-phosphide phase field at

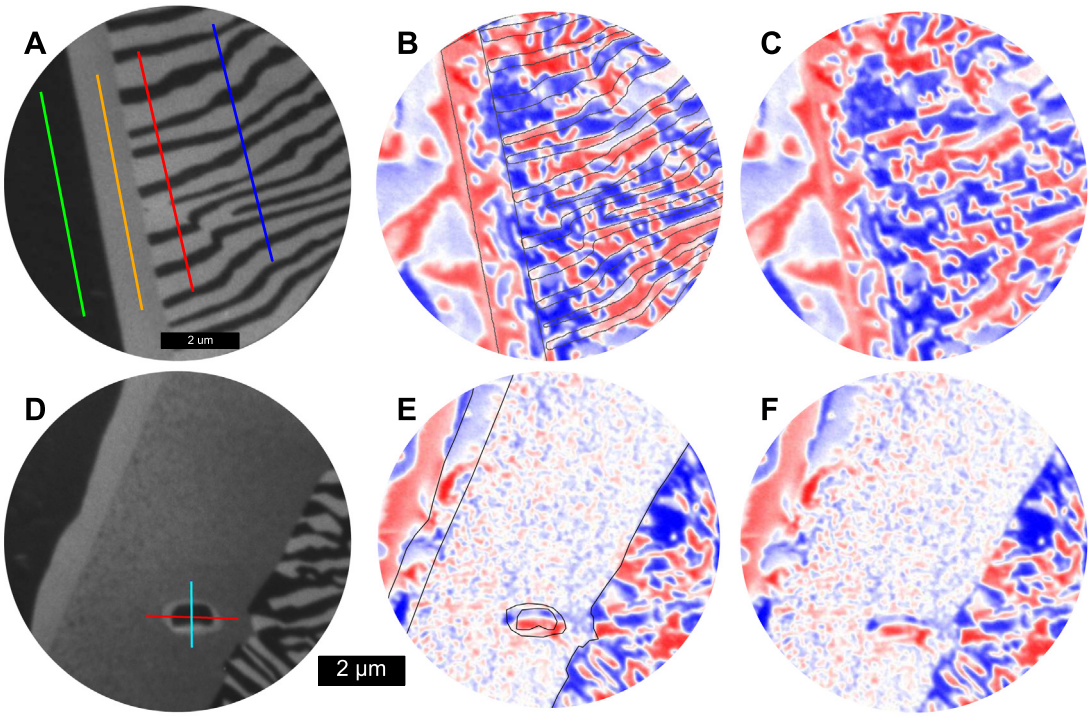

Fig. 9. (a) X-PEEM image of the Toluca meteorite, showing kamacite, tetrataenite rim and pearlitic plessite. Dark regions are Fe-rich and bright regions are Ni-rich. Compositional profiles corresponding to coloured lines are shown in Supplementary Material Fig. 7. (b) Overlay of compositional features from (a) on an image of the magnetisation of Toluca. The pearlitic plessite shows strong, multidomain magnetic behaviour. The intensity appears to be slightly higher in the Fe-rich regions than the Ni-rich regions. (c) Magnetisation image of Toluca without compositional overlay. (d) X-PEEM image of the Odessa meteorite, showing kamacite, tetrataenite rim, cloudy zone, a kamacite rhomb with tetrataenite rim within the cloudy zone and pearlitic plessite. Dark regions are Fe-rich and bright regions are Ni-rich. Coloured lines refer to compositional profiles shown in Supplementary Material Fig. 9. (e) Overlay of compositional features from (d) on an image of the magnetisation of Odessa. The contrast between the magnetisation of the cloudy zone compared to the pearlitic plessite is striking. The intensity of magnetisation in the pearlitic plessite is much stronger, more comparable with the multidomain kamacite. (f) Magnetisation image of Odessa corresponding X-PEEM image (d). (For interpretation of the references to colour in this figure legend, the reader is referred to the web version of this article.)

400 °C. Kowalik et al. (1988) have investigated pearlitic plessite in three IAB irons: Canyon Diablo, Odessa and Toluca. They suggest that the pearlitic plessite forms with the KS orientation relationship between individual lamellae at $T < 400$°C in residual taenite regions with >23 wt% Ni. The relationship between pearlitic plessite and the Widmanstätten structure is interpreted as a high-angle boundary for lamellar nucleation in P-depleted regions. Brooks and Perrin (1995) suggest that the lamellae coarsen over time, with coarse lamellae having a different orientation to the fine lamellae. In a subsequent paper, Brooks and Fitch (2000) show evidence for the lamellae being kamacite and tetrataenite, suggesting slow cooling rates of 1–100 °C Myr^{-1} and formation of lamellae at the eutectoid reaction $\gamma \rightarrow \alpha + \gamma_2$ at $T \sim 405$ °C (Table 2). They do not, however, suggest a mechanism for how/why pearlitic plessite forms. We discuss below in Section 4.2 a potential mechanism for pearlitic plessite formation based on our EBSD results.

A recent study (Goldstein et al., 2017) highlights the importance of the presence of C in iron meteorites exhibiting pearlitic and spheroidised plessite. They investigated three MG and three sLL IAB iron meteorites and demonstrated that, although they show characteristic M-shaped diffusion profiles, their C content is much more heterogeneous. At 500 °C, C diffusion is $\sim 10^9$ times faster than Ni, suggesting that C is much more sensitive to decomposition reactions at lower temperatures. These much faster diffusion rates could help in the formation of pearlitic and

Table 2
Definitions of the symbols and abbreviations used to describe the microstructures and orientational relationships.

Symbol	Associated Microstructure
α	First generation of kamacite
α_{W1}	First generation of kamacite Widmanstätten lamellae
α_{W2}	Second generation of kamacite Widmanstätten lamellae
α'	Martensite
γ	Taenite above the Curie temperature
γ_2	Taenite below the Curie temperature
K	Kamacite
TT	Tetrataenite
CZ	Cloudy Zone
P	Pearlitic Plessite
S	spheroidised Plessite
NB	Neumann Bands

Table 3
List of common orientation relationships, used in the analysis (Nolze and Geist, 2004; Nolze, 2004).

Orientation Relationship	Definition of Misorientation
Kurdjumov-Sachs (K-S)	$(1\,1\,1)_\gamma \| (0\,1\,1)_\alpha, [\bar{1}\,0\,1]_\gamma \| [\bar{1}\,\bar{1}\,1]_\alpha$
Nishiyama-Wassermann (N-W)	$(1\,1\,1)_\gamma \| (0\,1\,1)_\alpha, [1\,1\,\bar{2}]_\gamma \| [0\,\bar{1}\,1]_\alpha$
Pitsch (P)	$(0\,1\,0)_\gamma \| (1\,0\,1)_\alpha, [1\,0\,1]_\gamma \| [\bar{1}\,1\,1]_\alpha$
Bain (B)	$(0\,1\,0)_\gamma \| (0\,1\,0)_\alpha, [1\,0\,1]_\gamma \| [1\,0\,1]_\alpha$

spheroidised plessite, although Goldstein et al. (2017) note that pearlitic plessite is in fact depleted in C. There is a clear correlation between high C content and the presence of pearlitic and spheroidised plessite in iron meteorites, however this observation does not help to constrain the formation mechanism of these microstructures.

The analysed areas of pearlitic and spheroidised plessite presented in this study are not associated with unusually high concentrations or precipitates of either P (Fig. S4) or C (Fig. S3), although we note that bulk sample contains an abundance of rhabdite crystals (Fig. S8) and nearby schreibersite (Fig. S10). We cannot comment, therefore, on the direct role that C and P might play in the formation mechanism of either pearlitic or spheroidised plessite.

An extensive study of twenty-two L chondrites attempted to relate the degree of shock, using classification based on silicates, to constrain the conditions leading to the formation of pearlitic plessite (Bennett and McSween, 1996). They found evidence of fine-grained pearlitic plessite in the Tennasilm and Jhung chondrites, which have experienced S3 shock metamorphism. The Jhung chondrite has been estimated to have been shock reheated to >475 °C. Pearlitic plessite is also observed in the Tenham and Kyushu chondrites, which experienced S4 and S5 degree shock, respectively. Coarse grained pearlite is associated with a higher degree of shock, and is observed in the Kingfisher L5 chondrite (Taylor and Heymann, 1970) which is thought to have experienced post-shock reheating of >600 °C.

Although we find little evidence for the high shock levels reported by Bennett and McSween (1996), there are several lines of evidence suggesting that plastic deformation occurred either at or below the formation temperature of fine pearlitic plessite in Odessa and Toluca. Both show Neumann bands, a type of mechanical twin that form on {1 1 2} planes (Fig. S14) (Pappu and Murr, 2000). Neumann bands typically form in larger grains of kamacite at low temperatures, since in these larger grains the shear is more easily accommodated by mechanical twins than by slip (Uhlig, 1955). Uhlig (1955) suggest that this type of shock deformation is only observed following the formation of the Widmanstätten pattern, consistent with a late-stage impact following slow cooling. The observed subgrains of kamacite (Fig. 7) may be related to dislocation networks formed by recovery after plastic deformation caused by an impact, although it is not clear whether the extent of plastic deformation was sufficient to generate a significant increase in dislocation density. The presence of fine-scale, branching magnetic domains in the kamacite suggests shock may have caused stress-induced anisotropy in the magnetic domain configuration of the kamacite (Fig. S12) (Moskowitz et al., 1988; Cerruti and Zapperi, 2007; Uspenskaya et al., 2010). In other meteorites, such as the pallasites, the interfaces between each Fe-Ni microstructure are typically straight, running perpendicular to the M-shaped Ni diffusion profile (Bryson et al., 2015; Nichols et al., 2016). In Toluca and Odessa, we observe significant perturbations to these interfaces (Fig. 2). The kamacite – tetrataenite rim interface exhibits a wavy morphology, and in some cases the kamacite crosses all the way through the tetrataenite rim and pierces the cloudy zone (Fig. 2g). The tetrataenite rim – cloudy zone boundary is also wavy in places, but the perturbations are less pronounced. We interpret these interface defects as clear evidence for plastic deformation post-dating the formation of the tetrataenite rims.

Although the presence of low-degree shock features suggest an impact affected the parent body after cooling to below 400 °C (and therefore could have played a role in triggering the finest phase of pearlitic plessite formation), it is unlikely that another impact could also have triggered the coarser generations of pearlitic plessite, which would have formed at a higher temperature. A causal link between an impact and the generation of the finest pearlitic plessite is possible, therefore, but not proved.

4.2. A potential mechanism for the formation and evolution of pearlitic and spheroidised plessite

Our EBSD measurements are the first to reveal the detailed crystallographic architechture of both pearlitic and spheroidised plessite, providing the opportunity to test theories about how each microstructure originated and evolved. The formation of any type of plessite requires the transformation of a single-phase parental taenite into a two-phase intergrowth of kamacite and taenite. There are three different mechanisms by which this could be achieved, each with its own unique microstructural and crystallographic characteristics:

1. Continuous Precipitation: This refers to the homogeneous nucleation of kamacite lamellae, accompanied by the development of Ni-rich rims and M-shaped diffusion profiles in the surrounding parental taenite. Each kamacite lamella adopts one of the possible Widmanstätten orientations (Fig. 4), and the Ni-rich rims retain the parental taenite orientation (yellow in Fig. 3). The kamacite/taenite boundary is KS.
2. Discontinuous Precipitation: This refers to the transformation of parental taenite into a lamellar intergrowth of kamacite and taenite behind an advancing reaction front (Manna et al., 2001; Zięba, 2017). Discontinuous precipitation is characterised by the reaction $\gamma_0 \rightarrow \alpha + \gamma$ where γ_0 is the residual taenite grain, which breaks down to form taenite lamellae (γ) with a distinct composition and crystallographic orientation interspersed with kamacite lamellae (α). Both the composition and the crystallographic orientation of taenite change abruptly across the reaction front. A KS relationship is expected at the interface between kamacite and taenite within the lamellar

intergrowth, but no orientation relationship is expected between the lamellar phases and the parental taenite across the reaction front. The kinetics of discontinuous precipitation are enhanced by rapid diffusion of Fe and Ni along the reaction front. Discontinuous precipitation typically initiates at a grain boundary in the parental phase, where there is significant lattice mismatch. However, examples discontinuous precipitation initiating from more coherent boundaries are well documented (Manna et al., 2001).

3. Martensitic decomposition: This process refers to the diffusionless transformation of low-Ni taenite into an iso-chemical mixture of bcc martensite laths in a parental taenite matrix, followed by the diffusion of Ni out of the martensite and into the surrounding taenite. Taenite retains the crystallographic orientation of the parental taenite. The martensite laths adopt one of the Widmanstätten orientations. Some small laths of taenite may later exsolve from the martensite with a different crystallographic orientation (Goldstein and Michael, 2006). Typically, the formation of plessite via this mechanism leads to multiple orientations of kamacite domains with a range of textures (acicular, comb, net, cellular, finger, black, duplex, etc.) intergrown with uniformly oriented taenite with a low-energy orientation relationship between the two (Goldstein and Michael, 2006). These characteristic textures enable martensitic decomposition to be distinguished from continuous precipitation.

Continuous precipitation is evident throughout the retained taenite region on a range of lengths scales, and is responsible for the multiple generations of Widmanstätten kamacite (labelled αw_1 and αw_2 in Fig. 3), as well as the small rhomb-shaped kamacite precipitates seen in the cloudy zone (Fig. 2).

The finest generation of pearlitic plessite displays all the necessary feaures of discontinuous precipitation. The perpendicular contact between the tetrataenite rim and fine-scale pearlitic plessite is evidence that pearlitic plessite nucleated on the tetrataenite rim, and that the discontinuous precipitation reaction front advanced from there into the surrounding taenite (Figs. 2a and 9a). The uniform thickness of the tetrataenite rim, and the sharpness of the tetrataenite rim/pearlitic plessite interface (Fig. 9a) implies that the rim was well established before nucleation of pearlitic plessite took place. This observation is consistent with the idea that cooling to $T < 400\,^{\circ}C$ occured before nucleation of pearlitic plessite took place. Colonies of lamellae nucleated in random orientations with respect to the parental taenite (Fig. 5). Each colony displays a KS relation between the lamellar kamacite and taenite, but an irregular orientation relationship to the parental taenite. The boundary between the fine pearlite and the cloudy zone represents the final position reached by the reaction front as the temperature cooled to the point that discontinuous precipitation could no longer proceed. The morphology of the reaction front is often highly irregular, and clearly affected by the presence of pre-existing kamacite precipitates (Figs. 1 and 2d, e, and f).

Coarse pearlitic plessite is seen around the edges of the large region of retained taenite. The coarsest regions appear to initiate directly from the kamacite/taenite boundary, so likely formed at a higher temperature (i.e. at $T > 400\,^{\circ}C$), before the formation of the rim. In most other regions, however, there is a small region of cloudy zone, followed by irregular, rounded raft-like regions of high-Ni taenite, followed by a slighter finer generation of coarse pearlite. The pearlite is interspersed with more irregular rafts of high-Ni taenite, some of which are adjacent Widmanstätten kamacite, but others that appear isolated. The irregular rafts all have the parental taenite orientation. Throughout the coarse pearlite, there is a uniform kamacite orientation and two distinct orientations of pearlitic taenite lamellae.

Towards the centre of the residual taenite grain, Ni content continues to decrease, therefore the ratio of kamacite to taenite lamellae increases. In these regions pearlitic plessite gives way to form spheroidised plessite. Spheroids have been observed in the Ocotillo (IAB) and Arispe (IC) iron meteorites (Brooks, 2000). Spheroidisation is well understood in steel pearlite, and is often associated with Ostwald ripening of fine-scale lamellar integrowths during slow cooling (Chattopadhyay and Sellars, 1982). It has previously been suggested that spheroidised plessite forms by the coarsening of defects within pearlitic plessite (Brooks, 2000).

Given their retained parental taenite orientation, formation of the irregular rafts and spheroids by coarsening of pre-existing discontinuous precipitation lamellae, as suggested most recently by Goldstein et al. (2017), can be categorically ruled out. Retention of a parental taenite orientation is a feature of both the continuous precipitation and martensitic decomposition mechanisms. However, both these mechanisms predict kamacite orientations and kamacite-taenite orientation relationships that are inconsistent with observations throughout the retained taenite region. Therefore, none of the three mechanisms above can adequately explain the crystallographic architechture of the coarse pearlite and spheroidised plessite regions.

Here we propose a new mechanism for the formation of irregular raft and spheroidal taenite that can explain all the observed features. The mechanism generates a mixture of pearlitic plessite and Ni-enriched patches of parental taenite during the progression of the reaction front, followed by later coarsening to form spheroidal plessite (Fig. 11).

Stage 1 (Fig. 11a): discontinuous precipitation initiates at the kamacite/taenite boundary. An irregular reaction front progresses into the retained taenite, resulting in coarse pearlite.
Stage 2 (Fig. 11b): discontinuous precipitation is facilitated by Fe-Ni diffusion along the reaction front, but if the temperature is high enough then volume diffusion is also possible on the length scale necessary to enrich and stabilise a region of parental taenite ahead of the reaction front. Lobes of kamacite advance, and gradually isolate the Ni-enriched taenite patch.
Stage 3 (Fig. 11c): With further advancement, the reaction front rejoins itself and a rounded raft of Ni-rich taenite with the retained taenite crystallographic orienta-

tion becomes isolated. Continued progress of the reaction front leads to renucleation of taenite lamellae (allowing a switch of taenite orientation in some cases). Stage 4 (Fig. 11d): Coarsening occurs by the removal of taenite lamellae, feeding the growth of the taenite raft into a larger spheroid, driven by the overall decrease in surface energy. This process could continue to completion, removing all thin taenite lamellae and leaving behind a uniformly oriented kamacite with taenite spheroids.

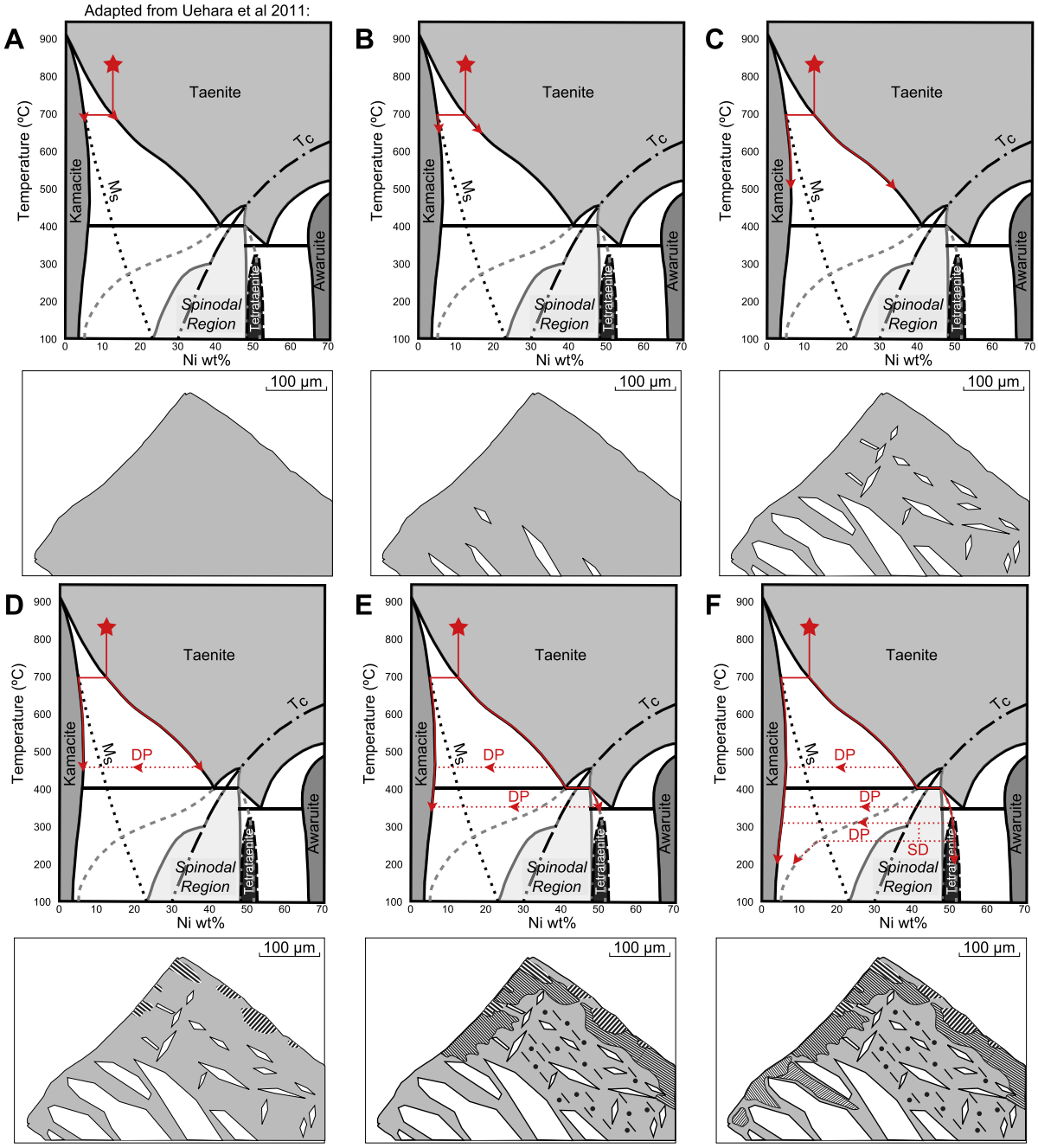

Fig. 10. Phase diagrams and schematic diagrams for the slow cooling of the IAB irons. (a) Nucleation of kamacite (pale region in schematic diagram) concentrates Ni-rich residual taenite into small regions (darker region in schematic diagram). (b) A second region of kamacite lamellae nucleate upon further cooling. (c) A third generation of kamacite lamellae. These are distinguishable by their smaller size in comparison to the second generation, which have now coarsened. (d) Coarse pearlitic plessite nucleates on the kamacite-taenite boundary and begins to propagate into the residual taenite grain. The pearlitic plessite forms by discontinuous precipitation. (e) A second generation of discontinuous precipitation occurs. Fine pearlitic plessite nucleates on the coarse pearlitic plessite and the tetrataenite rim. In Ni-rich regions large rafts of Ni-rich taenite become isolated. In the central region of the residual taenite grain where Ni contents is lower spheroidised plessite forms. Mechanisms for the growth of these microstructures are shown in Fig. 11. (f) Fine pearlitic plessite forms by discontinuous precipitation is the most Ni-rich regions. The remaining residual taenite decomposes to cloudy zone via spinodal decomposition.

The lack of both irregular rafts and spheroids in the fine pearlite regions may be explained by the observation that fine pearlite formed at lower temperatures, where the rate of volume diffusion is lower. In addition, the closer spacing of the lamellae in fine pearlite may be less favourable towards the bowing mechanism, since it would require a much higher curvature of reaction front.

4.3. Thermal history of the IABs from chemical and crystallographic observations

The compositions of the microstructures observed in Odessa are used to reconstruct the microstructural evolution of the IABs using the Fe-Ni phase diagram (Fig. 10). We have also considered the Fe-Ni-C and Fe-Ni-P systems (Romig and Goldstein, 1978; Hopfe and Goldstein, 2001). The IABs are reported to be rich in C (Goldstein et al., 2017); Odessa contains 2 wt% C (Buchwald, 1975). The high percentage of rhabdite crystals in the matrix (Fig. S8) also suggests the Fe-Ni system is P-saturated. Fig. 10 uses the Fe-Ni phase diagram, since this is best experimentally constrained for a broad range of temperatures and Ni compositions (Yang et al., 1996). We show the presence of P and C make a minimal difference to the temperature of microstructural transformations (Fig. S13).

There are three distinct size distributions of kamacite, which we interpret as three separate nucleation events. Kamacite is the first phase to nucleate at ~700 °C, concentrating the residual Ni into regions of taenite (Fig. 10a). The second generation of kamacite is identified by the presence of large lamellae with a width of ~50–100 μm within the retained taenite region (Fig. 10b). The third generation of kamacite lamellae then develops with widths less than ~10 μm (Fig. 10c).

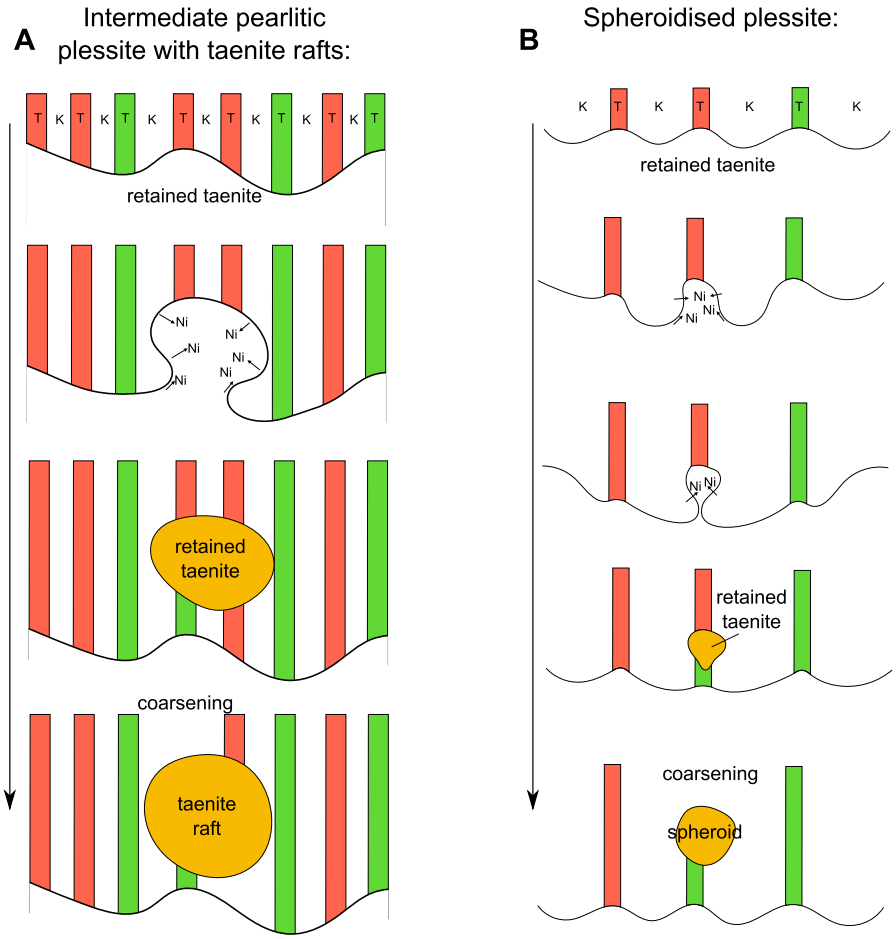

Fig. 11. We present a new mechanism by which isolated rafts and spheroids of Ni-rich taenite can form, whilst maintaining the same crystallographic orientation as the parent taenite grain (Fig. 3). Due to their crystallographic orientation, they cannot form by direct coarsening of pearlitic plessite. The taenite lamellae and spheroids are depicted using the same colour scheme as in the EBSD images. (a) In the pearlitic plessite near the tetrataenite rim, where Ni concentrations are still high, large rafts of Ni-rich taenite are observed. We suggest that the reaction front which forms pearlitic plessite by discontinuous precipitation does not proceed at a constant rate. The reaction front acts as a fast conduit for diffusion, allowing Ni to concentrate in the regions where the reaction front moves slowest. This isolates regions of residual taenite which then become enriched in Ni compared to the rim and cloudy zone. (b) We propose a similar mechanism to that discussed in (a), however further from the tetrataenite rim, Ni content is lower and retained taenite undergoes a martensitic transformation to form kamacite. This allows more effective spheroidisation to take place, and the taenite lamellae become discontinuous as the majority of excess Ni is now trapped within the spheroids.

All kamacite formed by nucleation and growth from parental taenite or retained taenite is surrounded by an M-shaped diffusion profile, and the kamacite-taenite boundary displays the expected low-energy KS orientation relationship. The presence of well-defined tetrataenite rims, followed in many places by cloudy zone, is evidence that slow cooling continued without disruption to temperatures <400 °C (Fig. 10d and e).

Nucleation of coarse pearlitic plessite occured at multiple locations along the kamacite-taenite interface (Fig. 10d). Once nucleated, domains of pearlitic plessite propagated into the residual taenite grain. With further cooling, a second generation of intermediate pearlitic plessite formed (Fig. 10d) and the reaction front progressed towards the centre of the retained taenite. Irregular rafts of Ni-rich taenite form via the bowing mechanism within the intermediate pearlitic plessite (Fig. 11a–d). Discontinuous precipitation continues throughout the interior of the retained taenite, creating a mixture of pearlite lamellae and taenite spheroids (Fig. 11e–i). Coarsening of spheroids, at the expense of the taenite lamellae, leads to localised partial or complete transition into spheroidised plessite. A uniform kamacite orientation is observed throughout, except in regions that were not accesible by the main reaction front due to occlusion by pre-existing Widmanstätten lamellae.

The last microstructures to form during slow cooling are fine pearlitic plessite and the cloudy zone. The cloudy zone forms by spinodal decomposition. Typically spinodal decomposition energetically inhibits discontinuous precipitation in iron meteorites, preventing the development of pearlitic plessite (Manna et al., 2001). Spinodal decomposition and discontinuous precipitation can occur simultaneously within a grain (Zięba, 2017). It is unclear whether the cloudy zone or the fine pearlitic plessite formed first, however some experimental results suggest discontinuous precipitation occurs at higher temperatures, and spinodal decomposition is then initiated at lower temperatures (Zhao and Notis, 1999), following the cessation of the advancement of the reaction front.

4.4. Paleomagnetic implications

The lack of magnetic field recorded by Odessa and Toluca is unsurprising, given the unusual formation of these iron meteorites in a planetesimal mantle, rather than in a metallic core (Ruzicka, 2014; Weiss et al., 2017). Even if the parent body had an incipient core, it is highly unlikley it would have the convective power to drive a dynamo so long after the time of accretion >25 Myr, based on cooling rate estimates) (Elkins-Tanton et al., 2011). This is consistent with the geochemical and petrological assessment of the IABs, which suggest that the metal most likely formed in metallic pools, distributed throughout the parent body following an impact event that scrambled the planetesimal during differentiation (Benedix et al., 2000; Wasson and Kallemeyn, 2002). Therefore we may conclude either that the IAB parent body did not have a metallic core, or its incipient core was unable to drive a dynamo at the time of cloudy zone formation.

5. CONCLUSIONS

High-resolution X-ray and electron microscopy imaging, combined with detailed EBSD analysis, provide the most detailed study to date on the characterisation and formation mechanism for pearlitic and spheroidised plessite.

Multiple generations of pearlitic plessite formed by discontinuous precipitation of kamacite and taenite from the residual taenite host. In most iron meteorites, this is kinetically unfavourable compared to the formation of the cloudy zone by spinodal decomposition. Discontinuous precipitation accounts for the abrupt change in composition and crystallographic orientation between the pearlitic plessite and retained taenite.

The spheroids in spheroidised plessite have the same crystallographic orientation as the cloudy zone and tetrataenite rim, suggesting they all originate from the retained taenite grain. This provides conclusive evidence that spheroidisation does not occur by coarsening of pre-existing pearlitic plessite, as previously reported in the literature. We propose a new mechanism for spheroidisation, in which the reaction front of propagating pearlitic plessite traps portions of the residual taenite grain, maintaining its original orientation. Subsequent coarsening of the pre-formed spheroids, at the expense of the pearlite lamellae, leads to either partial or complete transformation to spheroidised plessite.

We propose that pearlitic and spheroidised plessite development require slow cooling. The presence of carbon is also evidently important, since pearlitic plessite and spheroidised plessite are only observed in carbon-rich irons (Buchwald, 1975; Kowalik et al., 1988; Goldstein et al., 2017). The presence of carbon alone however does not provide an obvious mechanism for the formation of these microstructures.

An impact event on the IAB parent body after slow cooling and formation of the Widmanstätten pattern is supported by evidence for low-temperature deformation. We observed both microstructural and magnetic evidence for deformation; principally the irregular nature of microstructural interfaces, the presence of Neumann bands, and fine-scale, branching magnetic domain walls in kamacite. This impact event follows the initial large impact that scrambled the parent body, redistributing the metal throughout (Ruzicka, 2014).

Paleomagnetic analysis of the cloudy zone suggests the IAB parent body did not experience a significant magnetic field generated by a core dynamo at the time of cloudy zone formation. This is in agreement with the hypothesis that the IAB parent body was unable to form a significant metallic core.

ACKNOWLEDGEMENTS

We thank Ed Scott, Tim McCoy and Patrick Donohue for very helpful review comments which provided a significant contribution to the interpretation of this data. We also acknowledge Giulio Lampronti for assistance with EBSD data acquisition. This work was supported by the European Research Council under the European Union's Seventh Framework Programme (FP/2007-2013)/ ERC grant agreement numbers 320750 and 312284. RK acknowl-

edges Rolls-Royce plc, the EPSRC and the BMWi under grants EP/H022309/1, EP/H500375/1 and 20T0813. JHA acknowledges financial support from the Spanish MINECO MAT2014-53921-R and Aragonese DGA-IMANA E34, both cofunded by Fondo Social Europeo and European Union FEDER funds. We acknowledge the Helmholtz-Zentrum Berlin for the use of the synchrotron radiation beam time at beamline UE49 of BESSY II. We thank the Sedgwick Museum, University of Cambridge for samples.

APPENDIX A. SUPPLEMENTARY MATERIAL

Supplementary data associated with this article can be found, in the online version, at https://doi.org/10.1016/j.gca.2018.03.009.

REFERENCES

Bachmann F., Hielscher R. and Schaeben H. (2010) Texture analysis with MTEX – free and open source software toolbox. *Solid State Phenom.* **160**, 63–68.

Benedix G. K., McCoy T. J., Keil K. and Love S. G. (2000) A petrologic study of the IAB iron meteorites: constraints on the formation of the IAB-Winonaite parent body. *Meteorit. Planet. Sci.* **35**, 1127–1141.

Benedix G., Haack H. and McCoy T. (2014) Iron and stony-iron meteorites. *Treatise Geochem.* **1**, 267–285.

Bennett M. E. and McSween H. Y. (1996) Shock features in iron-nickel metal and troilite of L-group ordinary chondrites. *Meteorit. Planet. Sci.* **31**, 255–264.

Brooks C. R. (2000) Microstructural observations of spheroidization from a lamellar structure in iron meteorites. *Mater. Charact.* **45**, 71–80.

Brooks C. R. and Fitch S. B. (2000) Transmission electron microscopy observations of the lamellar structure in the Arispe iron meteorite. *Mater. Charact.* **45**, 365–377.

Brooks C. R. and Perrin R. (1995) Microstructural observations and mechanisms of lamellar coarsening in iron meteorites. *Mater. Charact.* **35**, 229–243.

Bryson J. F., Church N. S., Kasama T. and Harrison R. J. (2014a) Nanomagnetic intergrowths in Fe–Ni meteoritic metal. The potential for time resolved records of planetesimal dynamo fields. *Earth Planet. Sci. Lett.* **388**, 237–248.

Bryson J. F., Herrero-Albillos J., Kronast F., Ghidini M., Redfern S. A., van der Laan G. and Harrison R. J. (2014b) Nanopaleomagnetism of meteoritic Fe–Ni studied using Xray photoemission electron microscopy. *Earth Planet. Sci. Lett.* **396**, 125–133.

Bryson J. F. J., Nichols C. I. O., Herrero-Albillos J., Kronast F., Kasama T., Alimadadi H., van der Laan G., Nimmo F. and Harrison R. J. (2015) Long-lived magnetism from solidification-driven convection on the pallasite parent body. *Nature* **517**, 472–475.

Buchwald V. F. (1975) *Handbook of iron meteorites*. University of California Press.

Bunge H. J. (1982) *Texture analysis in materials science: mathematical methods*, 1 Auflag. Butterworth & Co, London.

Cerruti B. and Zapperi S. (2007) Dynamic hysteresis from zigzag domain walls: discrete model and Monte Carlo simulations. *Phys. Rev. B – Condens. Matter Mater. Phys.* **75**, 1–9.

Chattopadhyay S. and Sellars C. (1982) Kinetics of pearlite spheroidisation during static annealing and during hot deformation. *Acta Metall.* **30**, 157–170.

Elkins-Tanton L. T., Weiss B. P. and Zuber M. T. (2011) Chondrites as samples of differentiated planetesimals. *Earth Planet. Sci. Lett.* **305**, 1–10.

Forman L., Bland P., Timms N., Daly L., Benedix G., Trimby P., Collins G. and Davison T. (2017) Defining the mechanism for compaction of the CV chondrite parent body. *Geology* **45**.

Frank F. C. (1988) Orientation mapping. *Metall. Trans. A* **19**, 403–408.

Goldstein J. I., Huss G. R. and Scott E. R. (2017) Ion microprobe analyses of carbon in Fe–Ni metal in iron meteorites and mesosiderites. *Geochim. Cosmochim. Acta* **200**, 367–407.

Goldstein J. I. and Michael J. R. (2006) The formation of plessite in meteoritic metal. *Meteorit. Planet. Sci.* **41**, 553–570.

Goldstein J. I., Scott E. R. D. and Chabot N. L. (2009) Iron meteorites: crystallization, thermal history, parent bodies, and origin. *Chem. Erde Geochem.* **69**, 293–325.

Goldstein J. I., Yang J. and Scott E. R. (2014) Determining cooling rates of iron and stony-iron meteorites from measurements of Ni and Co at kamacite taenite interfaces. *Geochim. Cosmochim. Acta* **140**, 297–320.

Greenwood R. C., Franchi I. A., Gibson J. M. and Benedix G. K. (2012) Oxygen isotope variation in primitive achondrites: the influence of primordial, asteroidal and terrestrial processes. *Geochim. Cosmochim. Acta* **94**, 146–163.

Harrison R. J., Bryson J. F. J., Nichols C. I. O. and Weiss B. (2017) Magnetic mineralogy of meteoritic metal: paleomagnetic evidence for dynamo activity on differentiated planetesimals. In *Planetesimals: early differentiation and consequences for planets*. Cambridge University Press Kapitel 10, pp. 204–223.

Hetherington M. G., Jakubovics J. P., Szpunar J. A. and Tanner B. K. (1987) High-voltage Lorentz electron microscopy studies of domain structures and magnetization processes in pearlitic steels. *Philos. Mag. Part B* **56**, 561–577.

Hopfe W. D. and Goldstein J. I. (2001) The metallographic cooling rate method revised: application to iron meteorites and mesosiderites. *Meteorit. Planet. Sci.* **36**, 135–154.

Horan M., Smoliar M. and Walker R. (1998) 182W and 187Re-187Os systematics of iron meteorites: chronology for melting, differentiation, and crystallization in asteroids. *Geochim. Cosmochim. Acta* **62**, 545–554.

Kowalik J. A., Williams D. B. and Goldstein J. I. (1987) Formation of the lamellar structure in group IA and IIICD iron meteorites. In *Lunar and Planetary Science Conference*, vol. 18, pp. 511–512. Lunar and Planetary Science Conference.

Kowalik J. A., Williams D. B. and Goldstein J. I. (1988) Formation of the lamellar structure in group IA and IIID iron meteorites. In *Lunar and Planetary Science Conference*, vol. 18, pp. 493–501. Lunar and Planetary Science Conference.

Krakow R., Bennett R. J., Johnstone D. J., Vukmanovic Z., Solano-Alverez W., Lainé S. J., Einsle J. F., Midgley P. A., Rae C. M. F. and Hielscher R. (2017) On three-dimensional misorientation spaces. *Proc. R. Soc. A*, 473.

Kronast F., Schlichting J., Radu F., Mishra S. K., Noll T. and Dürr H. A. (2010) Spin-resolved photoemission microscopy and magnetic imaging in applied magnetic fields. *Surf. Interface Anal.* **42**, 1532–1536.

Labar J. L. and Torok S. (1992) A peak-to-background method for electron-probe X-ray microanalysis applied to individual small particles. *X-ray Spectrom.* **21**, 183–190.

Locatelli A. and Bauer E. (2008) Recent advances in chemical and magnetic imaging of surfaces and interfaces by XPEEM. *J. Phys.: Condens. Matter* **20**, 1–22.

Manna I., Pabi S. and Gust W. (2001) Discontinuous reactions in solids. *Int. Mater. Rev.* **46**, 53–91.

Morawiec A. (1997) Distributions of misorientation angles and misorientation axes for crystallites with different symmetries. *Acta Crystallogr. Sect. A Found. Crystallogr.* **53**, 273–285.

Moskowitz B. M., Halgedahl S. L. and Lawson C. A. (1988) Magnetic domains on unpolished and polished surfaces of titanium- rich titanomagnetite. *J. Geophys. Res.* **93**, 3372–3386.

Nichols C. I. O., Bryson J. F., Herrero-Albillos J., Kronast F., Nimmo F. and Harrison R. J. (2016) Pallasite paleomagnetism: quiescence of a core dynamo. *Earth Planet. Sci. Lett.* **441**, 103–112.

Nolting F., Scholl A., Stohr J., Seo J., Fompeyrine J., Siegwart H., Locquet J., Anders S., Luning J., Fullerton E., Toney M., Scheinfein M. and Padmore H. (2000) Direct observation of the alignment of ferromagnetic spins by antiferromagnetic spins. *Nature* **405**, 767–769.

Nolze G. (2004) Determination of orientation relationships between fcc/bcc lattices by the use of pole figures. In *HKL Usermeeting*, pp. 1–9.

Nolze G. and Geist V. (2004) A new method for the investigation of orientation relationships in meteoritic plessite. *Cryst. Res. Technol.* **39**, 343–352.

Ohldag H., Regan T., Stöhr J., Scholl A., Nolting F., Lüning J., Stamm C., Anders S. and White R. (2001) Spectroscopic identification and direct imaging of interfacial magnetic spins. *Phys. Rev. Lett.* **87**, 247201.

Pappu S. and Murr L. (2000) Shock deformation twinning in an iron explosively formed projectile. *Mater. Sci. Eng.: A* **284**, 148–157.

Pouchou J. L. and Pichoir F. (1991) Quantitative analysis of homogeneous or stratified microvolumes applying the model "PAP. In *Electron Probe Quantitation* (eds. Heinrich and Newbury). Plenum Press, New York, pp. 31–75.

Qin L., Dauphas N., Wadhwa M., Masarik J. and Janney P. E. (2008) Rapid accretion and differentiation of iron meteorite parent bodies inferred from 182Hf-182W chronometry and thermal modeling. *Earth Planet. Sci. Lett.* **273**, 94–104.

Rasmussen K. L. (1989) Cooling rates and parent bodies of iron meteorites from group IIICD, IAB, and IVB. *Phys. Scr.* **39**, 410–416.

Romig A. D. and Goldstein J. I. (1978) Determination of the Fe-rich portion of the Fe-Ni-C phase diagram. *Metall. Trans. A* **9**, 1599–1609.

Ruzicka A. (2014) Silicate-bearing iron meteorites and their implications for the evolution of asteroidal parent bodies. *Chem. Erde Geochem.* **74**, 3–48.

Schulz T., Upadhyay D., Münker C. and Mezger K. (2012) Formation and exposure history of non-magmatic iron meteorites and winonaites: Clues from Sm and W isotopes. *Geochim. Cosmochim. Acta* **85**, 200–212.

Scott E. R. D. and Bild R. W. (1974) Structure and formation of the San Cristobal meteorite, other IB irons and group IIICD. *Geochim. Cosmochim. Acta* **38**, 1379–1380.

Takeda H., Bogard D. D., Mittlefehldt D. W. and Garrison D. H. (2000) Mineralogy, petrology, chemistry, and 39Ar-40Ar and exposure ages of the Caddo County IAB iron: evidence for early partial melt segregation of a gabbro area rich in plagioclase-diopside. *Geochim. Cosmochim. Acta* **64**, 1311–1327.

Taylor G. J. and Heymann D. (1970) Electron microprobe study of metal particles in the Kingfisher meteorite. *Geochim. Cosmochim. Acta* **34**, 677–687.

Uehara M., Gattacceca J., Leroux H., Jacob D. and van der Beek C. J. (2011) Magnetic microstructures of metal grains in equilibrated ordinary chondrites and implications for paleomagnetism of meteorites. *Earth Planet. Sci. Lett.* **306**, 241–252.

Uhlig H. (1955) Contribution of metallurgy to the origin of meteorites. *Geochim. Cosmochim. Acta* **7**, 34–42.

Uspenskaya L., Nurgaliev T. and Miteva S. (2010) Temperature dependence of magnetization reversal of thin manganite film. *Acta Phys. Pol. A* **117**, 207–210.

Van Wilderen L. J. G. W., Offerman S. E., Van Dijk N. H., Rekveldt M. T., Sietsma J. and Van der Zwaag S. (2002) Neutron depolarization study of the austenite/pearlite phase transformation in steel. *Appl. Phys. A: Mater. Sci. Process.* **74**, 1052–1054.

Wasson J. T. and Kallemeyn G. W. (2002) The IAB iron-meteorite complex: a group, five subgroups, numerous grouplets, closely related, mainly formed by crystal segregation in rapidly cooling melts. *Geochim. Cosmochim. Acta* **66**, 2445–2473.

Weisberg M. K., Mccoy T. J. and Krot A. N. (2006) Systematics and evaluation of meteorite classification. In *Meteorites and the Early Solar System II* (eds. D. S. Lauretta and H. Y. McSween). University of Arizona Press, Tucson, pp. 19–52.

Weiss B. P., Wang H., Sharp T. G., Gattacceca J., Shuster D. L., Downey B., Hu J., Fu R. R., Kuan A. T., Suavet C., Irving A. J., Wang J. and Wang J. (2017) A nonmagnetic differentiated early planetary body. *Earth Planet. Sci. Lett.* **468**, 119–132.

Winfield T., Goldstein J. and Scott E. (2012) Cooling rate estimates for IAB and IIICD iron meteorites. In *43rd Lunar and Planetary Science Conference*, pp. 43–44.

Worsham E. A., Bermingham K. R. and Walker R. J. (2016) Siderophile element systematics of IAB complex iron meteorites: new insights into the formation of an enigmatic group. *Geochim. Cosmochim. Acta* **188**, 261–283.

Worsham E. A., Bermingham K. R. and Walker R. J. (2017) Characterizing cosmochemical materials with genetic affinities to the Earth: genetic and chronological diversity within the IAB iron meteorite complex. *Earth Planet. Sci. Lett.* **467**, 157–166.

Yang C., Williams D. and Goldstein J. (1996) A revision of the Fe-Ni phase diagram at low temperatures (<400 C). *J. Phase Equilib.* **17**, 522–531.

Yang J., Goldstein J. I. and Scott E. R. (2010) Main-group pallasites: thermal history, relationship to IIIAB irons, and origin. *Geochim. Cosmochim. Acta* **74**, 4471–4492.

Zhao J. C. and Notis M. R. (1999) Ordering transformation and spinodal decomposition in Au-Ni alloys. *Metall. Mater. Trans. A* **30A**, 707–716.

Zięba P. (2017) Recent developments on discontinuous precipitation. *Arch. Metall. Mater.* **62**, 955–968.

Associate editor: Alexander N. Krot